

Singlet-Doublet Majorana Dark Matter and Neutrino Mass in a minimal Type-I Seesaw Scenario

Manoranjan Dutta,^a Subhaditya Bhattacharya,^b Purusottam Ghosh,^c Narendra Sahu,^a

^a*Department of Physics, Indian Institute of Technology Hyderabad, Kandi, Telangana-502285, India.*

^b*Department of Physics, Indian Institute of Technology Guwahati, North Guwahati, Assam-781039, India.*

^c*Regional Centre for Accelerator-based Particle Physics, Harish-Chandra Research Institute, HBNI, Chhatnag Road, Jhansi, Allahabad - 211 019, India*

E-mail: ph18resch11007@iith.ac.in, subhab@iitg.ac.in, purusottamghosh@hri.res.in, nsahu@phy.iith.ac.in

ABSTRACT: In a bid to simultaneous explanation of dark matter (DM) and tiny but non-zero masses of left-handed neutrinos, we propose a minimal extension of the Standard Model (SM) by a vector-like fermion doublet and three right handed (RH) singlet neutrinos. The DM arises as a mixture of the neutral component of the fermion doublet and one of the RH neutrinos, both assumed to be odd under an additional \mathcal{Z}_2 symmetry. As a result, the DM emerges to be a dominantly Majorana particle and escapes from Z -mediated direct search constraints to mark a significant difference from singlet-doublet Dirac DM. The other two \mathcal{Z}_2 even heavy RH neutrinos give rise masses and mixing of light neutrinos via Type-I Seesaw mechanism. The particle content automatically allows us to extend the model by a gauged $U(1)_{B-L}$ symmetry, which is anomaly free and brings an additional portal between DM and SM particles. Relic density and direct search allowed parameter space for both the cases are investigated through detailed numerical scan, while collider search strategies are also indicated.

KEYWORDS: Dark matter, Neutrino mass, gauged $B - L$ symmetry.

Contents

1	Introduction	1
2	The Model for singlet-doublet Majorana DM	3
2.1	Masses and mixing of dark sector particles	4
2.2	Theoretical and Experimental constraints	6
3	Relic Abundance of singlet-doublet Majorana Dark Matter	6
3.1	Annihilation/Coannihilation processes and Boltzmann Equations	6
3.2	Parameter Space Scan	9
4	Direct Detection of singlet-doublet Majorana Dark Matter	12
5	Singlet-doublet Majorana DM in gauged $U(1)_{B-L}$ Extension of the SM	14
5.1	The Model	14
5.2	Spontaneous symmetry breaking and physical scalars	17
5.3	Masses and mixing of dark sector particles	18
5.4	Theoretical and Experimental constraints	20
5.5	Relic abundance of dark matter	20
5.6	Direct Detection prospects	22
5.7	ATLAS bound on $g_{BL} - M_{Z_{BL}}$	25
6	Collider Signatures	27
7	Non-zero masses and mixing of light neutrinos	34
8	Conclusion	38
A	DM-SM Interaction in model I	40
B	DM-SM Interaction in model II with $U(1)_{B-L}$ extension	41

1 Introduction

Astrophysical observations like galaxy rotation curves, gravitational lensing, Cosmic Microwave Background (CMB) acoustic fluctuations etc. provide compelling evidences towards the existence of Dark Matter (DM)[1, 2], a form of matter that is electromagnetically inert and hence extremely difficult to detect, but can be inferred from its gravitational affects. In fact, satellite borne experiments like WMAP and PLANCK [3, 4], which measure anisotropies in CMB, established that DM constitute almost 85% of the total matter content and 26.8%

of the total energy budget of the universe. Even after this tantalising hint, we have no answer to the question what DM actually is. DM as a fundamental particle answers many puzzles together like structure formation, self interaction, rotation curve etc., hence studied elaborately. Since no SM particle resembles the properties of a DM particle expected to have, it is believed that DM is essentially one or more particles beyond the Standard Model (BSM) content. Several BSM scenarios have been formulated to explain the particle nature of the DM, with additional field content and stabilising symmetry. Amongst different class of possibilities, Weakly Interacting Massive Particles (WIMP) has been the most popular due to its phenomenological richness, where DM can be explained as the thermal relics of the universe [5].

Another equally important puzzle in particle physics is the tiny neutrino mass which has been established by the solar and atmospheric neutrino oscillation experiments like T2K [6, 7], Double Chooz [8, 9], Daya Bay [10–12], Reno [13] and MINOS [14, 15]. Besides, the nature of neutrinos, whether Dirac or Majorana, is also not known. Neutrinoless double beta decay experiments [16] perhaps will shed light onto it. Within the SM, neutrinos are assumed massless with no right handed (RH) neutrinos. Even if RH neutrinos are incorporated to the SM, the required Yukawa coupling to explain sub-eV neutrino mass through spontaneous symmetry breaking via Dirac mass term turns out to be as tiny as 10^{-12} , almost six orders of magnitude smaller than the electron Yukawa coupling and seems pretty unnatural. Assuming that the neutrinos are Majorana, which violates lepton number by two units, the tiny neutrino masses can be realised via the dimension five gauge invariant effective Weinberg operator $LLHH/\Lambda$, where Λ denotes the scale of new physics and L, H are respectively the lepton and Higgs doublets of the SM [17]. After electroweak symmetry breaking (EWSB), the SM neutrinos acquire sub-eV masses given by $M_\nu = \langle H \rangle^2/\Lambda$. One possibility of generating this operator is to assume the presence of heavy RH neutrinos in the early universe, where the scale of new physics (Λ) is decided by the mass of RH neutrinos. Thus it is straightforward to see that for tiny neutrino mass of the order of $M_\nu \sim 0.1\text{eV}$, the new physics scale requires to be very heavy ($\Lambda \sim 10^{14}\text{GeV}$) when the involved couplings are of order one. This is usually referred as type-I seesaw mechanism [18–21].

While the origin of DM and neutrino mass is hitherto unknown, it is highly appealing and economical to find a model having simultaneous solution of both. In fact, such models are expected to have constrained parameter space in comparison to their individual counterpart and hence can be probed at ongoing and future terrestrial experiments. Motivated by this, here we consider a simple extension of the SM to explain simultaneously the sub-eV masses of neutrinos and DM content of the universe.

We consider a singlet-doublet WIMP like fermion DM [22–46]. The motivation of considering a singlet-doublet fermion DM has already been established; this is because a purely singlet case requires a higher dimensional effective operator for DM-SM interaction, which is mostly ruled out from direct search bound excepting for the Higgs resonance region, while the pure doublet case is also ruled out from relic density and direct search bound upto several TeVs of DM mass making the model inaccessible to probe. Our model consists of a vector-like fermion doublet $\Psi^T = (\psi^0, \psi^-)$ and three right handed neutrinos ($N_{R_i}, i = 1, 2, 3$). A \mathcal{Z}_2 symmetry is imposed under which the doublet Ψ and one of the right handed neutrinos, say

N_{R_1} are odd, while other particles are even. As a result there is mixing between the neutral component of the doublet and the singlet through the Yukawa interaction and DM emerges out to be a mixed state of the doublet ψ^0 and N_{R_1} after EWSB. Due to Majorana mass of the RH singlet N_{R_1} , the DM is dominantly a Majorana particle. As a result it escapes the Z -mediated vector current direct search interaction and provide a distinction from the earlier vector like singlet-doublet DM [40–45]. The field content permits us to extend the model easily to a gauged $U(1)_{B-L}$ scenario, which allows an additional gauge mediated interaction for DM. We find the relic density and direct search allowed parameter space for both the cases and also indicate possible collider search strategies. The neutrino mass arises from the Yukawa interaction of \mathcal{Z}_2 even RH neutrinos together with Majorana mass term in a minimal Type-I Seesaw framework. Since two RH neutrinos take part in the seesaw, one of the light neutrino mass is exactly zero. The masses of RH neutrinos, including the one which constitutes DM, originate from the $U(1)_{B-L}$ symmetry breaking scale. We assume their masses to be of same order and derive constraints from lepton flavour violating processes like $\mu \rightarrow e\gamma$.

The paper has been arranged as follows. In section-2, we explain the details of the model, followed by a summary of different theoretical and experimental constraints. We discuss the relic abundance of dark matter in section-3 and direct detection in section-4. Then we discuss the gauged $U(1)_{B-L}$ extension of the model in section-5. We briefly summarise collider search strategy for both the cases in section-6. In section-7, we discuss the light neutrino mass and finally conclude in section-8.

2 The Model for singlet-doublet Majorana DM

In this work the SM has been extended by one vector-like fermion doublet (VLFd) $\Psi^T = (\psi^0, \psi^-)$ (with hypercharge $Y = -1$, where we use $Q = T_3 + Y/2$) and three heavy right handed neutrinos (RHN) $N_{R_i} (i = 1, 2, 3)$, which are singlets under the SM gauge group. All the newly added particles are also singlet under $SU(3)_C$, i.e. colour neutral. An additional \mathcal{Z}_2 symmetry is imposed under which Ψ and N_{R_1} are odd, while all other fields are even. It is well known that the stability of DM is ensured by some additional symmetry and \mathcal{Z}_2 serves as the minimal one. The quantum numbers of the BSM fields under $SU(3)_c \times SU(2)_L \times U(1)_Y \times \mathcal{Z}_2$ are listed in Table 1. The Lagrangian of the model (as guided by Table 1) is given by:

$$\mathcal{L} = \mathcal{L}_{SM} + \bar{\Psi} (i\gamma^\mu D_\mu - M) \Psi + \overline{N_{R_i}} i\gamma^\mu \partial_\mu N_{R_i} - \left(\frac{1}{2} M_{R_i} \overline{N_{R_i}} (N_{R_i})^c + h.c.\right) + \mathcal{L}_{yuk}. \quad (2.1)$$

Apart from kinetic pieces, it is straightforward to note that since Ψ is a vector-like Dirac fermion, it possesses a bare Dirac mass term M , while all the three right handed neutrinos have Majorana mass M_{R_i} . Also worthy to note that D_μ denotes the covariant derivative involving the $SU(2)_L$ gauge boson triplet W_μ^a ($a = 1, 2, 3$) and $U(1)_Y$ gauge boson B_μ given by:

$$D_\mu = \partial_\mu - i\frac{g}{2}\tau_a W_\mu^a - ig'\frac{Y}{2}B_\mu; \quad (2.2)$$

where τ_a are Pauli spin matrices (generators of $SU(2)$), g and g' denote $SU(2)$ and $U(1)$ coupling strength respectively. This ensures that Ψ has $SU(2)$ gauge interaction with the SM.

Fields		$\underbrace{SU(3)_C \otimes SU(2)_L \otimes U(1)_Y}_{\mathcal{G}_{\text{SM}}} \otimes \mathcal{Z}_2$			
VLFd	$\Psi = \begin{pmatrix} \psi^0 \\ \psi^- \end{pmatrix}$	1	2	-1	-
RHNS	N_{R_1}	1	1	0	-
	N_{R_2}	1	1	0	+
	N_{R_3}	1	1	0	+
Higgs doublet	$H = \begin{pmatrix} w^+ \\ \frac{h+v+iz}{\sqrt{2}} \end{pmatrix}$	1	2	1	+

Table 1: Charge assignment of BSM fields with SM Higgs doublet under the gauge group $\mathcal{G} \equiv \mathcal{G}_{\text{SM}} \otimes \mathcal{Z}_2$ where $\mathcal{G}_{\text{SM}} \equiv SU(3)_C \otimes SU(2)_L \otimes U(1)_Y$.

We note that the Yukawa interaction plays the key role in this model and can be written as:

$$-\mathcal{L}_{yuk} = \left[\frac{Y_1}{\sqrt{2}} \bar{\Psi} \tilde{H} (N_{R_1} + (N_{R_1})^c) + h.c. \right] + \left(Y_{j\alpha} \bar{N}_{R_j} \tilde{H}^\dagger L_\alpha + h.c. \right). \quad (2.3)$$

where $\tilde{H} = i\tau_2 H^*$ and L denotes SM lepton doublet with indices $j = 2, 3$ and $\alpha = e, \mu, \tau$. N_{R_1} being odd under \mathcal{Z}_2 has Yukawa coupling to fermion doublet Ψ and determines the DM of the model after spontaneous symmetry breaking (SSB), as elaborated below. N_{R_2} and N_{R_3} being \mathcal{Z}_2 even, do not couple to Ψ , but couple to the SM lepton doublets and hence generate Dirac masses for SM neutrinos after SSB, which will be discussed in details later.

2.1 Masses and mixing of dark sector particles

Thanks to the Yukawa interaction given in 2.3, the electromagnetic charge neutral component of Ψ *viz.* ψ^0 and N_{R_1} mixes after the SM Higgs acquires vacuum expectation value (vev):

$\langle H \rangle = \frac{1}{\sqrt{2}} \begin{pmatrix} 0 \\ v \end{pmatrix}$. The mass terms for these fields can then be written together as:

$$-\mathcal{L}_{mass} = M \bar{\psi}_L^0 \psi_R^0 + \frac{1}{2} M_{R_1} \bar{N}_{R_1} (N_{R_1})^c + \frac{m_D}{\sqrt{2}} (\bar{\psi}_L^0 N_{R_1} + \bar{\psi}_R^0 (N_{R_1})^c) + h.c. \quad (2.4)$$

where $m_D = \frac{Y_1 v}{\sqrt{2}}$, where $v = 246$ GeV. Writing these mass terms in the basis $((\psi_R^0)^c, \psi_L^0, (N_{R_1})^c)^T$, we get the following mass matrix:

$$\mathcal{M} = \begin{pmatrix} 0 & M & \frac{m_D}{\sqrt{2}} \\ M & 0 & \frac{m_D}{\sqrt{2}} \\ \frac{m_D}{\sqrt{2}} & \frac{m_D}{\sqrt{2}} & M_{R_1} \end{pmatrix}. \quad (2.5)$$

In the above equation, assuming \mathcal{M} is symmetric,

it can be diagonalised by a single unitary matrix $\mathcal{U}(\theta) = U_{13}(\theta_{13} = \theta).U_{23}(\theta_{23} = 0).U_{12}(\theta_{12} = \frac{\pi}{4})$, which is essentially characterised by a single angle $\theta_{13} = \theta$. So we diagonalize the mass matrix \mathcal{M} by $\mathcal{U}.\mathcal{M}.\mathcal{U}^T = \mathcal{M}_{Diag.}$, where the unitary matrix \mathcal{U} is given by:

$$\mathcal{U} = \begin{pmatrix} 1 & 0 & 0 \\ 0 & e^{i\pi/2} & 0 \\ 0 & 0 & 1 \end{pmatrix} \begin{pmatrix} \frac{1}{\sqrt{2}} \cos \theta & \frac{1}{\sqrt{2}} \cos \theta & \sin \theta \\ -\frac{1}{\sqrt{2}} & \frac{1}{\sqrt{2}} & 0 \\ -\frac{1}{\sqrt{2}} \sin \theta & -\frac{1}{\sqrt{2}} \sin \theta & \cos \theta \end{pmatrix}, \quad (2.6)$$

where the extra phase matrix is multiplied to make sure all the eigenvalues are positive.

The diagonalisation of the mass matrix 2.5 requires:

$$\tan 2\theta = \frac{2m_D}{M - M_{R_1}}. \quad (2.7)$$

The physical states that emerge are defined as $\chi_i = \frac{\chi_{iL} + (\chi_{iL})^c}{\sqrt{2}}$ ($i = 1, 2, 3$) and are related to the unphysical states as:

$$\begin{aligned} \chi_{1L} &= \frac{\cos \theta}{\sqrt{2}}(\psi_L^0 + (\psi_R^0)^c) + \sin \theta(N_{R_1})^c, \\ \chi_{2L} &= \frac{i}{\sqrt{2}}(\psi_L^0 - (\psi_R^0)^c), \\ \chi_{3L} &= -\frac{\sin \theta}{\sqrt{2}}(\psi_L^0 + (\psi_R^0)^c) + \cos \theta(N_{R_1})^c. \end{aligned} \quad (2.8)$$

All the three physical states χ_1, χ_2 and χ_3 are therefore of Majorana nature and their mass eigenvalues can be expressed respectively as,

$$\begin{aligned} m_{\chi_1} &= M \cos^2 \theta + M_{R_1} \sin^2 \theta + m_D \sin 2\theta, \\ m_{\chi_2} &= M, \\ m_{\chi_3} &= M_{R_1} \cos^2 \theta + M \sin^2 \theta - m_D \sin 2\theta. \end{aligned} \quad (2.9)$$

In the small mixing limit ($\theta \rightarrow 0$), the eigenvalues can be further simplified as,

$$\begin{aligned} m_{\chi_1} &\approx M + \frac{m_D^2}{M - M_{R_1}}, \\ m_{\chi_2} &= M, \\ m_{\chi_3} &\approx M_{R_1} - \frac{m_D^2}{M - M_{R_1}}. \end{aligned} \quad (2.10)$$

where we have assumed $m_D \ll M, M_{R_1}$. Hence it is clear that $m_{\chi_1} > m_{\chi_2} > m_{\chi_3}$ and χ_3 becomes the stable DM candidate. We may note here that the analysis taken up before in [40–45], where the \mathcal{Z}_2 odd doublet Ψ mixes with a *vector like singlet*, providing a Dirac DM state with one heavy electromagnetically charged Dirac state as opposed to two heavy Majorana states here.

Using the relation $\mathcal{U}\mathcal{M}\mathcal{U}^T = \mathcal{M}_{Diag.}$, one can express Y_1 , M and M_{R_1} in terms of the physical masses and the mixing angle as,

$$\begin{aligned} Y_1 &= \frac{\sqrt{2} \Delta M \sin 2\theta}{v}, \\ M &= m_{\chi_1} \cos^2 \theta + m_{\chi_3} \sin^2 \theta, \\ M_{R_1} &= m_{\chi_3} \cos^2 \theta + m_{\chi_1} \sin^2 \theta; \end{aligned} \tag{2.11}$$

where $\Delta M = (m_{\chi_1} - m_{\chi_3})$. We can also see that in the limit of $m_D \ll M$, $m_{\chi_1} \simeq m_{\chi_2} = M$, where M is the mass of electrically charged components ψ^\pm of vector-like fermion doublet Ψ . The phenomenology of dark sector is therefore governed mainly by the three independent parameters, DM mass, splitting with the heavier neutral component, and doublet-singlet mixing :

$$\text{Dark Parameters : } \{ m_{\chi_3}, \Delta M = (m_{\chi_1} - m_{\chi_3}) \approx (m_{\chi_2} - m_{\chi_3}), \sin \theta \}. \tag{2.12}$$

2.2 Theoretical and Experimental constraints

• **Perturbativity:** In order to maintain perturbativity of the model, Yukawa couplings should satisfy the following limits:

$$|Y_1| < \sqrt{4\pi}, \quad |Y_{\alpha j}| < \sqrt{4\pi} \quad . \tag{2.13}$$

• **LEP limits:** LEP exclusion bound on charged fermion mass $m_{\psi^\pm} = M > 102.7$ GeV [47]. The bound from LHC applies to a typical case of type III seesaw model, for which $m_{\psi^\pm} = M \gtrsim 800$ GeV [48, 49]. Note that we do not abide by the bound from LHC as the decay channels are widely different.

• **Relic Density and Direct Search of Dark Matter:** The observed number density of DM is constrained by the combined WMAP [3] and PLANCK [4] data as:

$$0.1166 \leq \Omega_{DM} h^2 \leq 0.1206. \tag{2.14}$$

For direct search, we have used the current stringent bounds from non-observation of DM at XENON-1T [50] ($\sim 10^{-47}$ cm²). We also note that the fluctuation recently observed at XENON 1T at \sim KeV scale [51] do not apply to our case.

3 Relic Abundance of singlet-doublet Majorana Dark Matter

3.1 Annihilation/Coannihilation processes and Boltzmann Equations

The basic assumption for calculation of relic density of the DM here is to assume that DM is in equilibrium with thermal bath due to its non-negligible interaction with the SM particles in the early universe. It thereafter ‘freezes out’ from the hot soup of the SM particles via the number changing processes through which DM number density depletes as the universe expands to provide correct relic density. The dark sector consists of DM χ_3 as well as heavy neutral components χ_1, χ_2 and charged components ψ^\pm (all odd under the dark symmetry \mathcal{Z}_2). The

number density of DM (χ_3) is therefore governed by its annihilation as well as coannihilations with other dark sector particles (χ_1, χ_2 and ψ^\pm) into SM final states. Feynman diagrams of relevant annihilation and coannihilation processes are shown in Fig. 1, Fig. 2 and Fig. 3. The DM-SM interaction terms which essentially contribute to the relic density has been detailed in Appendix A.

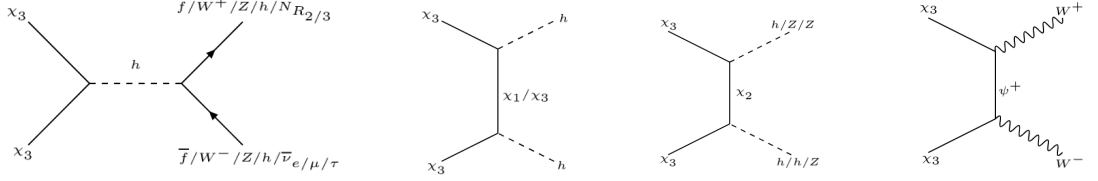


Figure 1: Annihilation channels to the SM through which the DM (χ_3) density depletes.

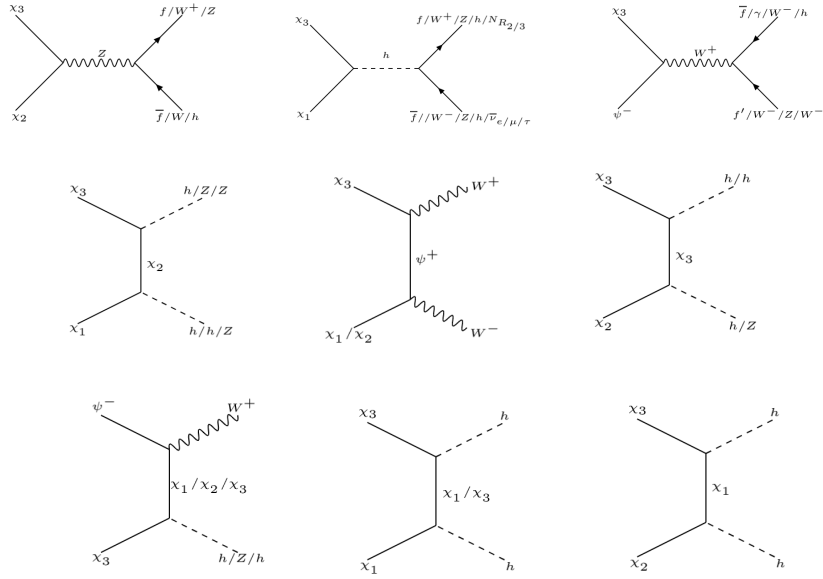


Figure 2: Coannihilation channels of DM (χ_3) with χ_1, χ_2 and ψ^\pm .

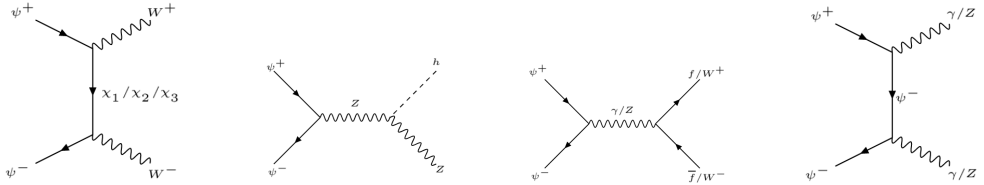


Figure 3: Annihilation channels of ψ^+ and ψ^- that contribute to coannihilation of DM (χ_3).

The relic density of DM in this scenario can be estimated by solving the Boltzmann

equation in the following form:

$$\frac{dn}{dt} + 3Hn = -\langle\sigma v\rangle_{eff} (n^2 - n_{eq}^2), \quad (3.1)$$

where n denotes number density of DM, i.e. $n \sim n_{\chi_3}$ and $n_{eq} = g(\frac{mT}{2\pi})^{3/2} \exp(-m/T)$ denotes equilibrium distribution, which DM is initially subjected to. Then it freezes out depending on $\langle\sigma v\rangle_{eff}$, which takes into account all number changing process listed in Fig. 1, Fig. 2 and Fig. 3 as well as those annihilations involving $\chi_{1,2}$ (although the contribution is very small) and can be estimated as follows:

$$\begin{aligned} \langle\sigma v\rangle_{eff} = & \frac{g_3^2}{g_{eff}^2} \langle\sigma v\rangle_{\bar{\chi}_3\chi_3} + \frac{2g_3g_2}{g_{eff}^2} \langle\sigma v\rangle_{\bar{\chi}_3\chi_2} \left(1 + \frac{\Delta M}{m_{\chi_3}}\right)^{\frac{3}{2}} \exp\left(-x \frac{\Delta M}{m_{\chi_3}}\right) \\ & + \frac{2g_3g_1}{g_{eff}^2} \langle\sigma v\rangle_{\bar{\chi}_3\chi_1} \left(1 + \frac{\Delta M}{m_{\chi_3}}\right)^{\frac{3}{2}} \exp\left(-x \frac{\Delta M}{m_{\chi_3}}\right) \\ & + \frac{2g_3g_4}{g_{eff}^2} \langle\sigma v\rangle_{\bar{\chi}_3\psi^\pm} \left(1 + \frac{\Delta M}{m_{\chi_3}}\right)^{\frac{3}{2}} \exp\left(-x \frac{\Delta M}{m_{\chi_3}}\right) \\ & + \frac{2g_2g_4}{g_{eff}^2} \langle\sigma v\rangle_{\bar{\chi}_2\psi^\pm} \left(1 + \frac{\Delta M}{m_{\chi_3}}\right)^3 \exp\left(-2x \frac{\Delta M}{m_{\chi_3}}\right) \\ & + \frac{2g_1g_4}{g_{eff}^2} \langle\sigma v\rangle_{\bar{\chi}_1\psi^\pm} \left(1 + \frac{\Delta M}{m_{\chi_3}}\right)^3 \exp\left(-2x \frac{\Delta M}{m_{\chi_3}}\right) \\ & + \frac{g_2^2}{g_{eff}^2} \langle\sigma v\rangle_{\bar{\chi}_2\chi_2} \left(1 + \frac{\Delta M}{m_{\chi_3}}\right)^3 \exp\left(-2x \frac{\Delta M}{m_{\chi_3}}\right) \\ & + \frac{g_1g_2}{g_{eff}^2} \langle\sigma v\rangle_{\bar{\chi}_1\chi_2} \left(1 + \frac{\Delta M}{m_{\chi_3}}\right)^3 \exp\left(-2x \frac{\Delta M}{m_{\chi_3}}\right) \\ & + \frac{g_1^2}{g_{eff}^2} \langle\sigma v\rangle_{\bar{\chi}_1\chi_1} \left(1 + \frac{\Delta M}{m_{\chi_3}}\right)^3 \exp\left(-2x \frac{\Delta M}{m_{\chi_3}}\right) \\ & + \frac{g_4^2}{g_{eff}^2} \langle\sigma v\rangle_{\psi^+\psi^-} \left(1 + \frac{\Delta M}{m_{\chi_3}}\right)^3 \exp\left(-2x \frac{\Delta M}{m_{\chi_3}}\right), \end{aligned} \quad (3.2)$$

where $\Delta M = m_i - m_{\chi_3}$ and m_i denotes the mass of χ_1 , χ_2 and ψ^\pm . Here we have defined g_{eff} as the effective degrees of freedom given by,

$$\begin{aligned} g_{eff} = & g_3 + g_2 \left(1 + \frac{\Delta M}{m_{\chi_3}}\right)^{\frac{3}{2}} \exp\left(-x \frac{\Delta M}{m_{\chi_3}}\right) \\ & + g_1 \left(1 + \frac{\Delta M}{m_{\chi_3}}\right)^{\frac{3}{2}} \exp\left(-x \frac{\Delta M}{m_{\chi_3}}\right) + g_4 \left(1 + \frac{\Delta M}{m_{\chi_3}}\right)^{\frac{3}{2}} \exp\left(-x \frac{\Delta M}{m_{\chi_3}}\right), \end{aligned} \quad (3.3)$$

where g_3 , g_2 , g_1 and g_4 are the internal degrees of freedom of χ_3 , χ_2 , χ_1 and ψ^\pm respectively. The dimensionless parameter x is defined as $x = \frac{m_{\chi_3}}{T}$. We also note that the contributions from processes which do not directly involve DM, like $\psi^+\psi^-$ in effective annihilation $\langle\sigma v\rangle_{eff}$ is further Boltzmann suppressed by $\exp(-2x \frac{\Delta M}{m_{\chi_3}})$. The relic density of the DM (χ_3) then can be given by [52],[53],[54]:

$$\Omega_{\chi_3} h^2 = \frac{1.09 \times 10^9 \text{GeV}^{-1}}{g_*^{1/2} M_{Pl}} \frac{1}{J(x_f)} \quad (3.4)$$

where $g_* = 106.7$ and $J(x_f)$ is given by

$$J(x_f) = \int_{x_f}^{\infty} \frac{\langle \sigma v \rangle_{eff}}{x^2} dx \quad . \quad (3.5)$$

Here $x_f = \frac{m_{\chi_3}}{T_f}$, where T_f denotes the freeze-out temperature of the DM. We may note here that for correct relic $x_f \simeq 20$.

It is worthy to mention here that we have adopted a numerical way of computing annihilation cross-section and relic density by inserting the model into the package `MicrOmegas` [55], where the model files are generated using another package `FeynRule` [56, 57].

3.2 Parameter Space Scan

In order to understand the DM relic density, let us first study the dependence on important relevant parameters: the mass of DM (m_{χ_3}), the mass splitting (ΔM) between the DM χ_3 and the next-to-lightest stable particle (NLSP) χ_2 and the mixing angle $\sin \theta$. Note that the charged components of Ψ namely ψ^\pm which contribute dominantly to the coannihilation channels has the same mass as that of χ_2 , *i.e.*, $m_{\chi_2} = m_{\psi^\pm}$. Variation of relic density of DM χ_3 is shown in Fig. 4 as a function of its mass for different choices of $\Delta M = 1-10$ GeV, 10-30 GeV, 30-50 GeV, 50-100 GeV shown by different colour shades as in the inset of the figure and for different choices of $\sin \theta = 0.01, 0.1, 0.3, 0.5$ in the top left, top right, bottom left and bottom right panels respectively.

As seen from Fig. 4, when ΔM is small, relic density is smaller due to large coannihilation contribution from flavour changing Z -mediated processes as well as W^\pm mediated processes (less Boltzmann suppression followed from Eq. 3.2). The resonance drops at $m_Z/2$ is seen due to s-channel off-diagonal Z mediated coannihilation interactions. As none of these neutral current interactions are diagonal, we observe the resonance to be somewhat flattened rather than a sharp spike that would have been expected if the interactions were diagonal. These coannihilation channels dominantly contribute towards the relic density as long as the mass splitting between the DM and NLSP is small, *e.g.*, for $\Delta M = 10$ GeV. As ΔM increases, these coannihilations become less and less effective, and Higgs mediated processes takes over. For $\Delta M = 30$ GeV, both contributions are present comparable while for $\Delta M > 30$ GeV, the contributions from vector current (coannihilation) interactions are practically negligible and the the Higgs mediated channel dominates. Consequently, we see a resonance drop at $m_h/2$, while the drop at $m_Z/2$ disappears. We have also observed that as long as ΔM is small and the coannihilation channels dominate, the effect of $\sin \theta$ on relic density is quite negligible. For smaller $\sin \theta$, the annihilation cross-section due to Higgs portal (see Eqn. A.3) is small leading to larger relic abundance, while for large $\sin \theta$, the effective annihilation cross-section is large leading to small relic abundance. However, this can only be observed when ΔM is sufficiently large enough and coannihilation processes are negligible. In Fig. 4, we also show the correct relic density by the silver horizontal line. In Fig. 5, the correct relic density allowed parameter space has been shown in the plane of ΔM vs m_{χ_3} for wide range of mixing angle $\{\sin \theta = 0.001 - 0.01, 0.01 - 0.1, 0.1 - 0.2, 0.2 - 0.4, 0.4 - 0.6\}$, indicated by different colours. We can see that in Fig. 5, there is a bifurcation around $\Delta M \sim 50$ GeV, so the allowed plane of $m_{\chi_3} - \Delta M$ are separated in two regions: (i) the bottom portion with small ΔM , where

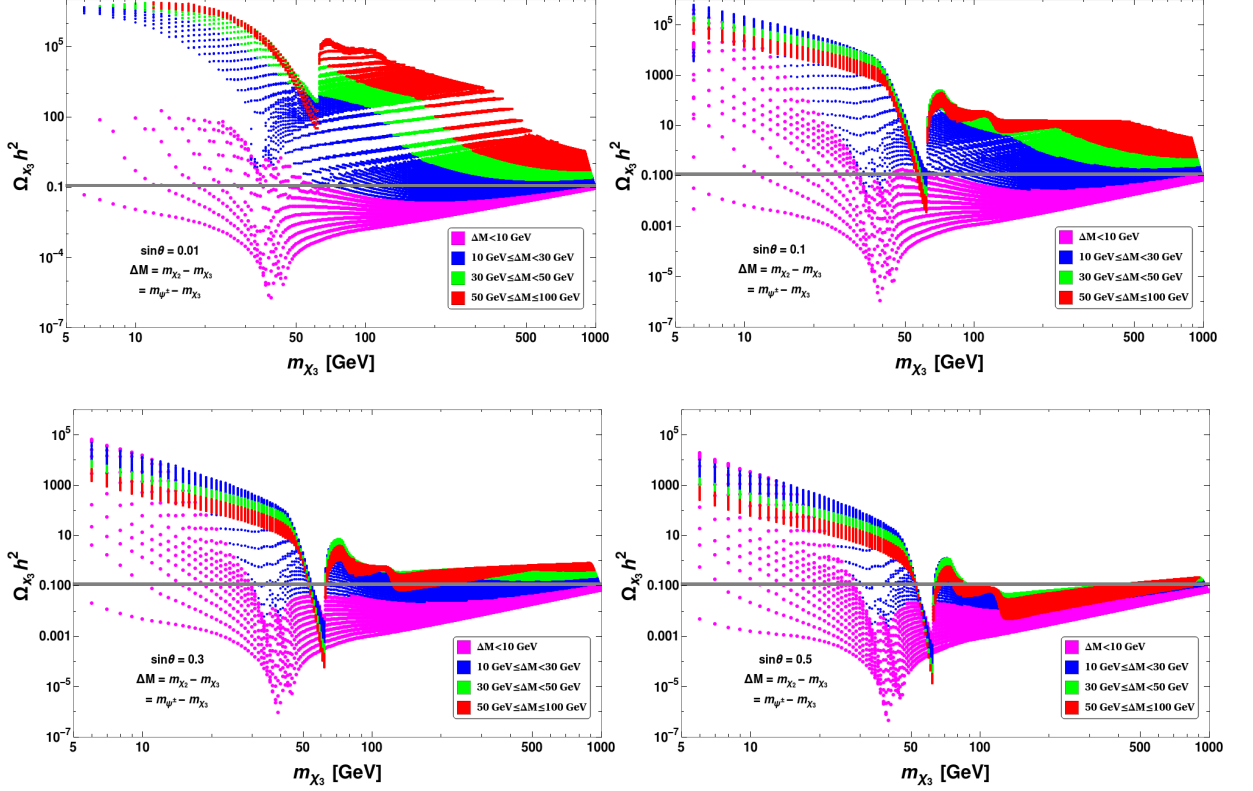


Figure 4: DM relic density as a function of DM mass (m_{χ_3}) for different mass splitting ΔM between the DM and the NLSP (as mentioned in figure inset in GeV) for $\sin\theta = 0.01$ (top left panel), $\sin\theta = 0.1$ (top right panel), $\sin\theta = 0.3$ (bottom left panel) and $\sin\theta = 0.5$ (bottom right panel). Correct relic density region from PLANCK data ($0.1166 \leq \Omega_{DM} h^2 \leq 0.1206$) is indicated by the silver horizontal line.

ΔM decreases with larger DM mass (m_{χ_3}) and (ii) the top portion of the figure with large ΔM , where ΔM increases slowly with larger m_{χ_3} .

In region (i), given a specific range of $\sin\theta$, the annihilation cross-section decreases with larger DM mass m_{χ_3} (from annihilation diagrams) and hence more co-annihilation contribution is required to get correct relic density, resulting ΔM to decrease. This also implies that the region below the each coloured zone is under-abundant (small ΔM implying large co-annihilation for a given m_{χ_3}), while the region above is over-abundant by the same logic. In this region the Yukawa coupling Y_1 which governs the annihilation cross-section is comparatively small since $Y_1 \propto \Delta M \sin\theta$ and ΔM is small. Also the annihilation cross-section decreases with increase in DM mass. Therefore, when DM mass is sufficiently heavy ($m_{\chi_3} > 1.2$ TeV), annihilation becomes too weak to be compensated by the coannihilation even when $\Delta M \rightarrow 0$, producing over abundance. Hence, for small ΔM , the allowed region has a maximum DM mass, as the region beyond $m_{\chi_3} \sim 1.2$ TeV is overabundant.

In region (ii), we note that, the co-annihilation contribution is much smaller due to large ΔM , so the annihilation processes effectively contribute to the relic density. Annihilation processes are essentially gauge or Higgs mediated. We already noted that Higgs Yukawa coupling

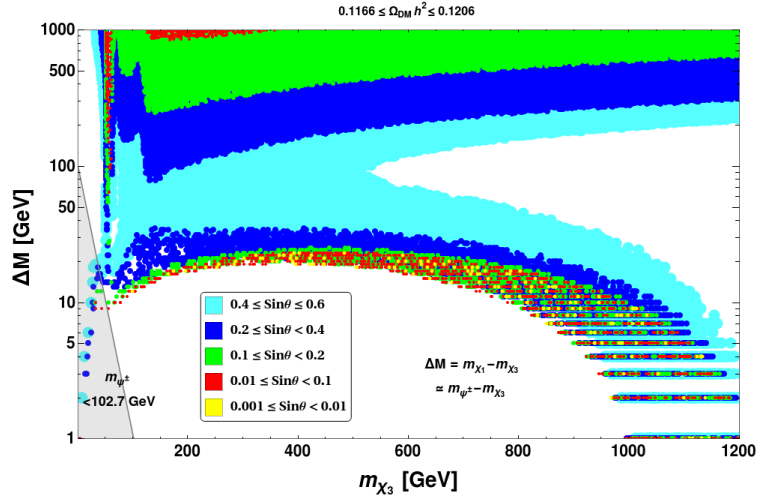


Figure 5: DM relic density ($0.1166 \leq \Omega_{DM} h^2 \leq 0.1206$) allowed parameter space in the plane of ΔM vs m_{χ_3} for different ranges of $\sin \theta$ as mentioned in the figure inset. The shaded region in the bottom left corner is ruled out by LEP exclusion bound on charged fermion mass, $m_{\psi^\pm} = M > 102.7$ GeV.

is proportional to both $\sin \theta$ and ΔM as $Y_1 \propto \Delta M \sin 2\theta$. Hence, for a given $\sin \theta$, larger ΔM leads to larger Y_1 and hence larger annihilation cross-section to yield under abundance, which can only be tamed down to correct relic density by having a larger DM mass. Also larger $\sin \theta$ requires smaller ΔM for the same reason. Therefore, the region above each coloured zone (allowed by relic density for a specific range of $\sin \theta$) is under abundant, while the region below each coloured zone is over abundant.

Let us come back to region (i) again and note that allowed parameter space indicates larger DM mass requires smaller and smaller ΔM and we reach a maximum DM mass (~ 1 TeV) for $\Delta M \rightarrow 0$. However, with $\Delta M \rightarrow 0$, the charged companions ψ^\pm are degenerate to DM and are stable. This is not acceptable as DM won't be dark then. Hence, ΔM can not be arbitrarily small. We can put a lower bound on ΔM by requiring the charged partners ψ^\pm of the DM to decay before the onset of Big Bang Nucleosynthesis ($\tau_{BBN} \sim 1$ sec.). The decay rate for the processes $\psi^\pm \rightarrow \chi_3 l^\pm \nu_l$ in the limit of small ΔM is given by ¹ :

$$\Gamma_{\psi^\pm} = \frac{1}{15(2\pi)^3} \frac{e^4 \sin^2 \theta (\Delta M)^5}{\sin^4 \theta_w M_W^4}, \quad (3.6)$$

By requiring that the charged fermions should decay before the onset of BBN, we can get a lower bound on ΔM as,

$$\tau_{\psi^\pm} = \frac{1}{\Gamma_{\psi^\pm}} \leq \tau_{BBN} \sim 1 \text{ sec} \implies \left(\frac{\Delta M}{\text{GeV}} \right)^5 \geq \frac{6.4 \times 10^{-13}}{\sin^2 \theta}. \quad (3.7)$$

In Fig. 6, we show the lower bound on ΔM for the range of $\sin \theta$ we used in our work. The region above the red line is allowed by the constraint. It is obvious that the bound is more stringent for smaller $\sin \theta$.

¹Semi-leptonic processes *e.g.* $\psi^\pm \rightarrow \chi_3 \pi^\pm$ are also possible, see for example [58]

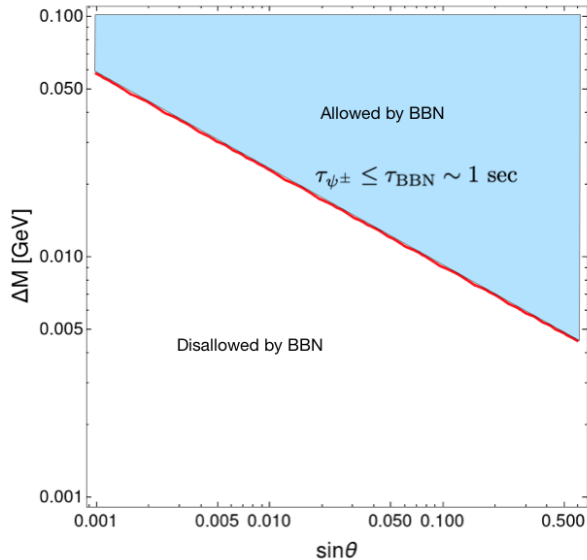


Figure 6: Lower bound on ΔM as a function of $\sin \theta$ from Big-Bang Nucleosynthesis (BBN). The shaded region is allowed.

4 Direct Detection of singlet-doublet Majorana Dark Matter

Among different possibilities of detecting DM, one major experimental procedure is direct DM search. Direct detection of the DM (χ_3) at a terrestrial laboratory is possible through elastic scattering of the DM off nuclei via Higgs-mediated interaction represented by the Feynman diagram shown in Fig. 7. The presence of only Higgs mediated diagram for direct

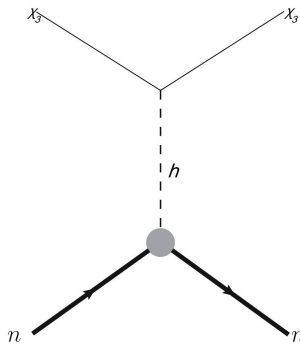


Figure 7: Feynman diagram for elastic scattering of DM off nuclei at terrestrial laboratory.

search makes this model crucially segregated from that of a vector like singlet-doublet DM as elaborated in [40–45]. Here, the DM being a Majorana fermion only has off diagonal Z-coupling and therefore do not contribute to direct search as it is very difficult to produce a heavier particle in the low energy scattering as in direct search experiment. The absence of Z mediation crucially alters the available parameter space of the model as we describe below. The corresponding vertex of $\chi_3 \chi_3 h$ can be obtained from the Lagrangian $\mathcal{L}_{DM-Higgs}$ given by Eq. A.3. The cross section per nucleon for the spin-independent (SI) DM-nucleon interaction

is then given by:

$$\sigma_{SI} = \frac{1}{\pi A^2} \mu_r^2 |\mathcal{M}|^2, \quad (4.1)$$

where A is the mass number of the target nucleus, μ_r is the reduced mass of the DM-nucleon system and \mathcal{M} is the amplitude for the DM-nucleon interaction, which can be written as:

$$\mathcal{M} = \left[Z f_p + (A - Z) f_n \right], \quad (4.2)$$

where f_p and f_n denote effective interaction strengths of DM with proton and neutron of the nuclei used for the experiment with A being mass number and Z being atomic number. The effective interaction strength can then further be decomposed in terms of interaction with parton as:

$$f_{p,n} = \sum_{q=u,d,s} f_{Tq}^{p,n} \alpha_q \frac{m_{(p,n)}}{m_q} + \frac{2}{27} f_{TG}^{p,n} \sum_{q=c,b,t} \alpha_q \frac{m_{(p,n)}}{m_q}; \quad (4.3)$$

with

$$\alpha_q = \frac{Y_1 \sin 2\theta m_q}{M_h^2 v} = \frac{\Delta M \sin^2 2\theta m_q}{v^2 M_h^2}; \quad (4.4)$$

coming from DM interaction with SM via Higgs portal coupling. Further, in Eq.4.3, the different coupling strengths between DM and light quarks are given by Bertone et al [1, 59] as $f_{Tu}^p = 0.020 \pm 0.004$, $f_{Td}^p = 0.026 \pm 0.005$, $f_{Ts}^p = 0.014 \pm 0.062$, $f_{Tu}^n = 0.020 \pm 0.004$, $f_{Td}^n = 0.036 \pm 0.005$, $f_{Ts}^n = 0.118 \pm 0.062$. The coupling of DM with the gluons in target nuclei is parameterised by:

$$f_{TG}^{(p,n)} = 1 - \sum_{q=u,d,s} f_{Tq}^{p,n}.$$

Using Eqs. 4.1, 4.2, 4.3 and 4.4, the spin-independent DM-nucleon cross-section is given by:

$$\sigma_{SI} = \frac{4}{\pi A^2} \mu_r^2 \frac{Y^2 \sin^2 2\theta}{M_h^4} \left[\frac{m_p}{v} \left(f_{Tu}^p + f_{Td}^p + f_{Ts}^p + \frac{2}{9} f_{TG}^p \right) + \frac{m_n}{v} \left(f_{Tu}^n + f_{Td}^n + f_{Ts}^n + \frac{2}{9} f_{TG}^n \right) \right]^2 \quad (4.5)$$

In the above equation for DM-nucleon direct search cross-section, two parameters from model that enter are the Higgs-DM Yukawa coupling (Y_1) and singlet-doublet mixing parameter ($\sin 2\theta$), which can be constrained by requiring that σ_{SI} is less than the current DM-nucleon cross-sections dictated by non-observation of DM in current direct search data. Recently, there has been a signal like event from electron recoil reported in XENON-1T data [51] observed at sub-GeV DM mass, which remains out of our scan.

In the left panel of Fig. 8, we confront the direct detection cross section obtained for the model as a function of DM mass, with bounds on spin-independent elastic scattering cross section from XENON-1T [50], shown by black dashed curve. It is worth mentioning that all points shown in left panel of Fig. 8 also satisfies relic density constraints from PLANCK. Different coloured patches indicate different ranges of mixing angle ($\sin \theta$) as indicated in figure panel. Obviously those regions that appear below the XENON-1T line can be allowed by the bound. It is obvious that Y_1 being proportional to $\sin \theta$ (see Eqn. 2.11) and due to the explicit presence of $\sin 2\theta$ in the direct search cross section as in Eq. 4.4, parameter space

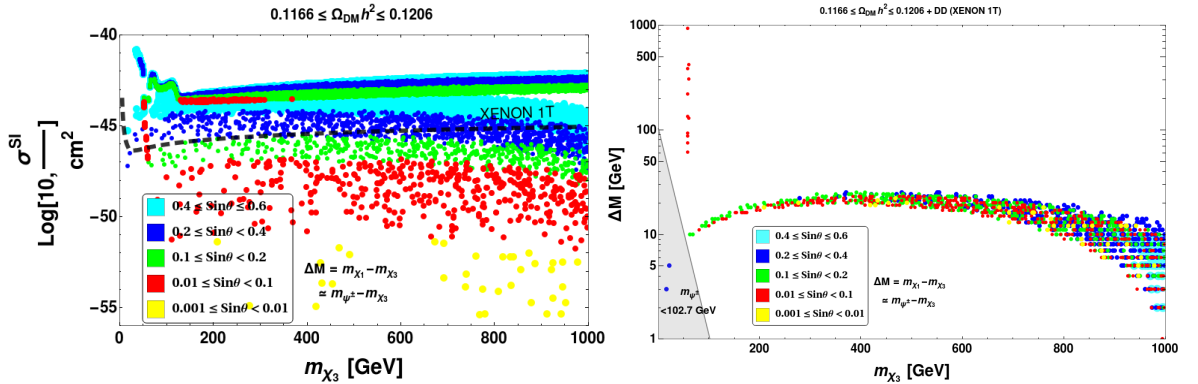


Figure 8: [Left]: Direct detection cross section for the DM (χ_3) confronted with bounds on spin-independent elastic scattering cross section by XENON-1T [50] over and above relic density constraint from PLANCK; [Right]: Correct DM relic density in $\Delta M - m_{\chi_3}$ plane constrained by XENON-1T bound. Different coloured points indicate different ranges of $\sin\theta$ as mentioned in figure inset. The shaded region in the bottom left corner of right panel plot is ruled out by LEP exclusion bound on charged fermion mass, $m_{\psi^\pm} = M > 102.7$ GeV.

with smaller $\sin\theta$ survive the cut. This is what is shown in $\Delta M - m_{\chi_3}$ plane in the right hand side (RHS) of Fig. 8, where we plot those points which simultaneously satisfy relic density [4] and direct search XENON-1T bound [50] together. It is seen that null observation from direct search crucially tames down the relic density allowed parameter space, which is evident when we compare the RHS of Fig. 8 with that of Fig. 5, where only relic density allowed parameter space is depicted. It is seen in RHS of Fig. 8, that $\sin\theta$ is correlated to DM mass and ΔM . For example, $\sin\theta$ is very small for smaller DM mass with moderate ΔM ($\sin\theta \lesssim 0.2$ for $m_{DM} \sim 500$ GeV with $\Delta M \sim 20$ GeV shown by red and green points); while larger $\sin\theta \sim 0.6$ is allowed at higher DM mass ~ 1000 GeV, with very small $\Delta M \lesssim 2$ GeV (Cyan points). This is simply because, the direct search cross-section is proportional to $\sim Y_1 \sin 2\theta \sim \Delta M \sin^2 2\theta$, therefore larger $\sin\theta$ requires ΔM to be smaller to remain within correct direct search limit. However, due to larger coannihilation contribution with small ΔM , the relic density drops below the PLANCK bound, unless we restore it to the correct ballpark by having larger DM mass (annihilation cross-section is inversely proportional to DM mass). This feature crucially distinguishes the model at hand from vector like singlet-doublet scenario with Dirac dark matter, where the presence of Z mediated direct search graph tames $\sin\theta$ to much smaller values like ~ 0.2 (for details see [40–45]). Higgs resonance $m_{\chi_3} \sim m_h/2$ is seen to satisfy both relic density and direct search bound, where ΔM can be very large having very small $\sin\theta \sim 0.2$.

5 Singlet-doublet Majorana DM in gauged $U(1)_{B-L}$ Extension of the SM

5.1 The Model

Due to the presence of three right handed neutrinos N_{R_i} and the fermion doublet Ψ being vector-like, the model is automatically $U(1)_{B-L}$ anomaly free if we assign one unit of B-L

charge to each of these fields. This is because of the fact that in a gauged B-L theory with only SM fermion content, non-zero anomalies are associated with the following two triangular diagrams:

$$\begin{aligned}\mathcal{A}_1[U(1)_{B-L}^3] &= \mathcal{A}_1^{SM}[U(1)_{B-L}^3] &= -3, \\ \mathcal{A}_2[(Gravity)^2 \times U(1)_{B-L}] &= \mathcal{A}_2^{SM}[(Gravity)^2 \times U(1)_{B-L}] &= -3,\end{aligned}\tag{5.1}$$

which are exactly cancelled by anomalies from three additional right handed neutrinos since,

$$\begin{aligned}\mathcal{A}_1^{RHN}[U(1)_{B-L}^3] &= 3 \\ \mathcal{A}_2^{RHN}[(Gravity)^2 \times U(1)_{B-L}] &= 3.\end{aligned}\tag{5.2}$$

Motivated by this fact, we extend the gauge group of the model to $SU(3)_C \times SU(2)_L \times U(1)_Y \times U(1)_{B-L} \otimes \mathcal{Z}_2$. Besides, one new complex scalar singlet Φ_{BL} is added with lepton number -2 . The particle content and the corresponding quantum numbers under the symmetry of the model are listed in the Table 2. Since two of the right handed neutrinos, say N_{R_2}, N_{R_3} are chosen to be even under the imposed \mathcal{Z}_2 symmetry, they can couple to the SM lepton and Higgs doublets to explain non-zero masses and mixing of light neutrinos. On the other hand, the vectorlike fermion doublet Ψ and N_{R_1} are chosen to be odd under the imposed \mathcal{Z}_2 symmetry. As a result the DM emerges as a mixture of the neutral component of the doublet Ψ *viz.* ψ^0 and N_{R_1} , similar to section 2. However, we notice certain differences in the mass matrix of dark sector neutral fermions in comparison to Eq. 2.5 due to the conservatoin of $B - L$ charge. In the following we discuss in details the corresponding phenomenology.

Fields		$\underbrace{SU(3)_C \otimes SU(2)_L \otimes U(1)_Y \otimes U(1)_{B-L} \otimes \mathcal{Z}_2}$				
VLFd	$\Psi = \begin{pmatrix} \psi^0 \\ \psi^- \end{pmatrix}$	1	2	-1	-1	-
RHNs	N_{R_1}	1	1	0	-1	-
	N_{R_2}	1	1	0	-1	+
	N_{R_3}	1	1	0	-1	+
Higgs doublet	$H = \begin{pmatrix} w^+ \\ \frac{h+v+iz}{\sqrt{2}} \end{pmatrix}$	1	2	1	0	+
Scalar Singlet	$\Phi_{BL} = \frac{\phi+v_{BL}+iz_\phi}{\sqrt{2}}$	1	1	0	-2	+

Table 2: Charge assignment of BSM fields along with the SM Higgs doublet under the gauge group $\mathcal{G} \equiv \mathcal{G}_{SM} \otimes U(1)_{B-L} \otimes \mathcal{Z}_2$, where $\mathcal{G}_{SM} \equiv SU(3)_C \otimes SU(2)_L \otimes U(1)_Y$.

Owing to the symmetry and charge assignments of the particles given in Tab. 2, the Lagrangian of the Model can be given as:

$$\mathcal{L} = \bar{\Psi}(i\not{D} - M)\Psi + \bar{N}_{R_i}i\not{D}N_{R_i} + \mathcal{L}_{yuk} + \mathcal{L}_{Gauge} + \mathcal{L}_{scalar} + \mathcal{L}_{SM};\tag{5.3}$$

where the covariant derivatives D_μ and \tilde{D}_μ are given by:

$$\begin{aligned} D_\mu &= \partial_\mu - i\frac{g}{2}\tau.W_\mu - ig'\frac{Y}{2}B_\mu - ig_{BL}Y_{BL}Z_{BL}, \\ \tilde{D}_\mu &= \partial_\mu - ig_{BL}Y_{BL}(Z_{BL})_\mu. \end{aligned} \quad (5.4)$$

In the covariant derivative of Ψ , there is an additional term due to the lepton number assignment, i.e. its transformation under $U(1)_{B-L}$; g_{BL} stands for $U(1)_{B-L}$ gauge coupling, which serves as a additional free parameter of the model. Note that Y_{BL} can simply be replaced by the lepton number assignment as given in Tab. 2.

The Yukawa interaction of the model is given by:

$$-\mathcal{L}_{yuk} = \left[Y_1 \bar{\Psi} \tilde{H} N_{R_1} + h.c. \right] + \left(Y_{j\alpha} \overline{N_{R_j}} \tilde{H}^\dagger L_\alpha + h.c. \right) + \left[\frac{y'_i}{2} \Phi_{BL} \overline{N_{R_i}} (N_{R_i})^c + h.c. \right]; \quad (5.5)$$

where $\alpha = e, \mu, \tau$, $j = 2, 3$ and $i = 1, 2, 3$. Due to $B-L$ conservation, the Yukawa interaction term $\bar{\Psi} \tilde{H} (N_{R_1})^c$ that was allowed in the earlier case (see Eqn. 2.3) is no longer allowed. For the same reason, the bare Majorana mass terms of right-handed neutrinos are also not allowed. The masses of right-handed neutrinos as well as the neutral gauge boson Z_{BL} are generated from the vev of Φ_{BL} . Thus the gauge sector is augmented by a new gauge boson Z_{BL} . The new gauge kinetic terms that appear in the Lagrangian constitute of,

$$\mathcal{L}_{Gauge} = -\frac{1}{4}(Z_{BL})_{\mu\nu}Z_{BL}^{\mu\nu} - \frac{\epsilon}{2}(Z_{BL})_{\mu\nu}B^{\mu\nu}; \quad (5.6)$$

where $Z_{BL}^{\mu\nu}$ represents the field strength of the $U(1)_{B-L}$ gauge boson and is defined as:

$$Z_{BL}^{\mu\nu} = \partial^\mu(Z_{BL})^\nu - \partial^\nu(Z_{BL})^\mu. \quad (5.7)$$

In the second term, ϵ parametrises the kinetic mixing between the $U(1)_{B-L}$ and $U(1)_Y$ gauge sectors. Such a mixing term can be generated through quantum corrections and approximated at one loop as $\epsilon \approx \frac{g'g_{BL}}{16\pi^2}$ [60, 61]. Since g_{BL} has tight upper bound from ATLAS, such one loop mixing is very very small compared to other relevant parameters of the model and the same has been neglected in rest of our analysis.

The Lagrangian of scalar sector is given by:

$$\mathcal{L}_{\text{scalar}} = |\mathcal{D}_\mu H|^2 + |\mathfrak{D}_\mu \Phi_{BL}|^2 - V(H, \Phi_{BL}) \quad (5.8)$$

where \mathcal{D}_μ and \mathfrak{D}_μ are given as follows:

$$\begin{aligned} \mathcal{D}_\mu &= \partial_\mu - i\frac{g}{2}\tau.W_\mu - ig'\frac{Y}{2}B_\mu \\ \mathfrak{D}_\mu &= \partial_\mu - ig_{BL}Y_{BL}(Z_{BL})_\mu. \end{aligned} \quad (5.9)$$

The scalar potential is given by

$$\begin{aligned} V(H, \Phi_{BL}) &= -\mu_H^2 \left(H^\dagger H \right) + \lambda_H \left(H^\dagger H \right)^2 \\ &\quad - \mu_\Phi^2 \left(\Phi_{BL}^\dagger \Phi_{BL} \right) + \lambda_\Phi \left(\Phi_{BL}^\dagger \Phi_{BL} \right)^2 + \lambda_{H\Phi} (H^\dagger H) \left(\Phi_{BL}^\dagger \Phi_{BL} \right). \end{aligned}$$

We note here that H do not have any transformation under the extended symmetry, while Φ_{BL} is a singlet under SM, the only gauge invariant terms that one can cook up are $H^\dagger H$ and $\Phi_{BL}^\dagger \Phi_{BL}$, resulting a simple scalar potential, where the only interaction term that can be written is $(H^\dagger H) (\Phi_{BL}^\dagger \Phi_{BL})$. $\lambda_{H\Phi}$ turns out to be an important additional parameter that contributes to the phenomenology. We also note that for both H and Φ_{BL} to acquire non-zero vevs, we need both μ_H and μ_Φ to be positive.

We analyse the model as follows: scalar mixing in subsection-5.2, masses and mixing of dark sector particles in subsection-5.3, theoretical and experimental constraints in subsection-5.4, relic abundance of DM in subsection-5.5, direct detection in subsection-5.6 and finally show the allowed parameter space in the light of ATLAS bound on g_{BL} versus $M_{Z_{BL}}$ in subsection 5.7.

5.2 Spontaneous symmetry breaking and physical scalars

At TeV scales Φ_{BL} acquires a non-zero vev and breaks $U(1)_{B-L}$ to identity. The non-zero vevs which spontaneously breaks $\mathcal{G}_{SM} \otimes U(1)_{B-L} \otimes \mathcal{Z}_2$ down to $U(1)_Q \otimes \mathcal{Z}_2$ are given as:

$$\langle \Phi_{BL} \rangle = \frac{v_{BL}}{\sqrt{2}}, \quad \langle H \rangle = \begin{pmatrix} 0 \\ \frac{v}{\sqrt{2}} \end{pmatrix}. \quad (5.10)$$

The minimization conditions around the vev's are given by :

$$\begin{aligned} \left. \frac{\partial V}{\partial H} \right|_v = 0 : \mu_H^2 &= \lambda_H v^2 + \frac{\lambda_{H\Phi} v_{BL}^2}{2}, \\ \left. \frac{\partial V}{\partial \Phi_{BL}} \right|_{v_{BL}} = 0 : \mu_\Phi^2 &= \lambda_\Phi v_{BL}^2 + \frac{\lambda_{H\Phi} v^2}{2}. \end{aligned} \quad (5.11)$$

Due to presence of $(H^\dagger H) (\Phi_{BL}^\dagger \Phi_{BL})$ interaction in the scalar sector, both weak states h and ϕ mix with each other. Using above minimization conditions, the mass terms of the scalar sector can be expressed as:

$$\begin{aligned} \mathcal{L}_{\text{scalar}}^{\text{mass}} &= \frac{1}{2} \begin{pmatrix} h & \phi \end{pmatrix} \begin{pmatrix} 2\lambda_H v^2 & \lambda_{H\Phi} v v_{BL} \\ \lambda_{H\Phi} v v_{BL} & 2\lambda_\Phi v_{BL}^2 \end{pmatrix} \begin{pmatrix} h \\ \phi \end{pmatrix}, \\ &= \frac{1}{2} \begin{pmatrix} h_1 & h_2 \end{pmatrix} \begin{pmatrix} m_{h_1}^2 & 0 \\ 0 & m_{h_2}^2 \end{pmatrix} \begin{pmatrix} h_1 \\ h_2 \end{pmatrix}. \end{aligned} \quad (5.12)$$

In order to obtain the mass eigenvalues, the flavor eigenstates are rotated by an orthogonal matrix as follows :

$$\begin{pmatrix} h_1 \\ h_2 \end{pmatrix} = \begin{pmatrix} \cos \beta & \sin \beta \\ -\sin \beta & \cos \beta \end{pmatrix} \begin{pmatrix} h \\ \phi \end{pmatrix}; \quad (5.13)$$

where h_1 and h_2 are the physical mass eigenstates. We identify h_1 to be the physical Higgs discovered in 2012 at LHC with mass $m_{h_1} = 125$ GeV and m_{h_2} remains a scalar beyond the SM. How heavy h_2 requires to be is constrained from LHC data which we discuss in a moment. The CP odd states also mix with each other, but turns out to be massless states known as

Goldstone Bosons. In unitary gauge they are accounted as the longitudinal modes of massive vector Bosons and do not enter into phenomenology explicitly. The scalar sector therefore accounts for three free parameters:

$$\{m_{h_2}, v_{BL}, \sin \beta\}; \quad (5.14)$$

which are constrained from Higgs data at Collider. We will discuss them in the next subsection. Other quartic couplings λ_H , λ_Φ and $\lambda_{H\Phi}$ can be expressed in terms of the physical parameters as:

$$\begin{aligned} \lambda_H &= \frac{m_{h_1}^2 \cos^2 \beta + m_{h_2}^2 \sin^2 \beta}{2v^2}, \\ \lambda_\Phi &= \frac{m_{h_1}^2 \sin^2 \beta + m_{h_2}^2 \cos^2 \beta}{2v^2}, \\ \lambda_{H\Phi} &= \frac{(m_{h_2}^2 - m_{h_1}^2) \sin 2\beta}{2vv_{BL}}. \end{aligned} \quad (5.15)$$

The broken $U(1)_{B-L}$ gauge symmetry yields mass for Z_{BL} as:

$$M_{Z_{BL}} = 2g_{BL}v_{BL} \quad (5.16)$$

$M_{Z_{BL}}$ and g_{BL} are constrained from both LEP and LHC which we shall address later. So it follows from Eqn. 5.16 that v_{BL} is no longer a free parameter. Instead, in the combined gauged and scalar sector, the free parameters involved are:

$$\{m_{h_2}, M_{Z_{BL}}, g_{BL}, \sin \beta\}; \quad (5.17)$$

As we will see in the later sections, these parameters play a crucial role in DM phenomenology in the $U(1)_{B-L}$ extension of the SM model.

5.3 Masses and mixing of dark sector particles

After electroweak symmetry breaking the mass term of the neutral dark sector particles can be written as,

$$-\mathcal{L}_{mass} = M\overline{\psi}_L^0\psi_R^0 + \frac{1}{2}M_{R_1}\overline{N}_{R_1}(N_{R_1})^c + m_D\overline{\psi}_L^0N_{R_1} + h.c., \quad (5.18)$$

where $m_D = \frac{Y_1\langle v \rangle}{\sqrt{2}}$ with $\langle v \rangle = 246$ GeV being the vacuum expectation value (vev) of the SM Higgs H and $M_{R_i} = \frac{y'_i v_{BL}}{\sqrt{2}}$, where v_{BL} is the vev of new scalar Φ_{BL} . Writing these mass terms in the basis $((\psi_R^0)^c, \psi_L^0, (N_{R_1})^c)^T$, we get the mass matrix:

$$\mathcal{M} = \begin{pmatrix} 0 & M & 0 \\ M & 0 & m_D \\ 0 & m_D & M_{R_1} \end{pmatrix}. \quad (5.19)$$

The above mass matrix of neutral dark sector particles can be diagonalized by using an orthogonal transformation: $\mathcal{M}_{diag} = U\mathcal{M}U^T$, where $U = U_{13}(\theta_{13})\cdot U_{23}(\theta_{23})\cdot U_{12}(\theta_{12})$ and

$U_{13}(\theta_{13})$, $U_{23}(\theta_{23})$ and $U_{12}(\theta_{12})$ are taken as three Euler rotation matrices. Assuming $m_D \ll M, M_{R_1}$, the mass eigenvalues are given by ²:

$$\begin{aligned} m_{\chi_1} &\approx M + \frac{m_D^2}{2(M - M_{R_1})}, \\ m_{\chi_2} &\approx -\left(M + \frac{m_D^2}{2(M + M_{R_1})}\right), \\ m_{\chi_3} &\approx M_{R_1} \left(1 - \frac{m_D^2}{M^2 - M_{R_1}^2}\right). \end{aligned} \quad (5.20)$$

From Eqs. (5.19) and (5.20) we see that $\text{Tr}\mathcal{M} = M_{R_1} = \sum_{i=1}^3 m_{\chi_i}$. Note that the above diagonalization is upto $\mathcal{O}(\frac{m_D^2}{M+M_{R_1}})$. The corresponding physical eigenstates can be given in terms of flavour eigenstates as:

$$\begin{aligned} \chi_{1L} &= (c_{13}c_{12} + s_{13}s_{23}s_{12})(\psi_R^0)^c + (c_{13}s_{12} - s_{13}s_{23}c_{12})\psi_L^0 + (s_{13}c_{23})N_{R_1}^c, \\ \chi_{2L} &= (-c_{23}s_{12})(\psi_R^0)^c + (c_{23}c_{12})\psi_L^0 + s_{23}N_{R_1}^c, \\ \chi_{3L} &= (-s_{13}c_{12} + c_{13}s_{23}s_{12})(\psi_R^0)^c + (-s_{13}s_{12} - s_{23}c_{12}c_{13})\psi_L^0 + (c_{13}c_{23})N_{R_1}^c. \end{aligned} \quad (5.21)$$

where we abbreviated $\cos\theta_{ij} = c_{ij}$ and $\sin\theta_{ij} = s_{ij}$, with $\{ij : 12, 13, 23\}$. The diagonalisation of the mass matrix requires:

$$\begin{aligned} \theta_{12} &= \frac{\pi}{4}, \\ \tan 2\theta_{23} &= \frac{-\sqrt{2}m_D}{M + M_{R_1}}, \\ \tan 2\theta_{13} &= \left(\frac{\sqrt{2}m_D}{M - M_{R_1} - \frac{m_D^2}{2(M+M_{R_1})}}\right) \cos\theta_{23}. \end{aligned} \quad (5.22)$$

Thus in the effective theory the dark sector comprises of three physical Majorana fermions χ_1, χ_2, χ_3 defined as $\chi_i = \frac{\chi_{iL} + (\chi_{iL})^c}{\sqrt{2}}$ ($i = 1, 2, 3$). We assume $m_{\chi_1} > m_{\chi_2} > m_{\chi_3}$, so that χ_3 serves as a stable dark matter candidate. In the limit $m_D \ll M, M_{R_1}$, from Eq. 5.22, we can further write,

$$Y_1 \approx \frac{\Delta M \sin 2\theta_{13}}{v}, \quad (5.23)$$

where $\Delta M = |m_{\chi_1}| - |m_{\chi_3}| \approx |m_{\chi_2}| - |m_{\chi_3}|$. The mixing angle θ_{23} can be obtained using values of m_D in the definition of θ_{13} . Therefore the phenomenology of dark sector is governed mainly by the following three independent parameters: DM mass m_{χ_3} , splitting with the heavier neutral components ΔM and mixing angle θ_{13} . Thus the ultimate free parameters in the dark sector are:

$$\text{Dark Parameters : } \{ m_{\chi_3}, \Delta M, \sin\theta_{13} \}, \text{ or } \{ M_{R_1}, M, \sin\theta_{13} \}. \quad (5.24)$$

²Similar to Eqn. 2.6, the mass matrix 5.19 can be further rotated by a phase matrix U_{ph} to make sure all the eigenvalues are positive.

5.4 Theoretical and Experimental constraints

• **Stability of potential:** In order to maintain stable vacuum, the quartic terms of the scalar potential should obey following co-positivity conditions [62, 63]:

$$\lambda_H \geq 0, \quad \lambda_\Phi \geq 0 \quad \text{and} \quad \lambda_{H\Phi} + 2\sqrt{\lambda_H \lambda_\Phi} \geq 0. \quad (5.25)$$

• **Perturbativity:** In order to maintain perturbativity of the model, Yukawa couplings should satisfy the following limits:

$$\begin{aligned} |\lambda_H| < 4\pi, \quad |\lambda_\Phi| < 4\pi, \quad |\lambda_{H\Phi}| < 4\pi \quad ; \\ |Y_1| < \sqrt{4\pi}, \quad |Y_{\alpha j}| < \sqrt{4\pi}, \quad |g_{BL}| < \sqrt{4\pi} \quad . \end{aligned} \quad (5.26)$$

• **LEP limits:** LEP exclusion bound on charged fermion mass, $m_{\psi^\pm} = M > 102.7$ GeV [47]. Again, we note that the bound from LHC has been evaluated for a typical case of type III seesaw model, $m_{\psi^\pm} = M \gtrsim 800$ GeV [48, 49], which is not strictly applicable to our case.

• **Constraints on $M_{Z_{BL}}$:** LEP II data puts lower bound on $M_{Z_{BL}}/g_{BL} \geq 7$ TeV [64]. Corresponding bound from ATLAS and CMS at LHC Run 2 is more severe than LEP II, $M_{Z_{BL}} > 4.3$ TeV for g_{BL} of the same order as that of SM coupling [65–67]. However, this constraint can be relaxed for lower value of g_{BL} . For $M_{Z_{BL}} = \mathcal{O}(1\text{TeV})$, the upper bound on g_{BL} can be as small as 0.009 [68].

• **Bounds on scalar singlet transforming under $U(1)_{B-L}$:** In the extended scalar sector, the mixing angle ($\sin\beta$) and the mass of the extra physical state (m_{h_2}) faces the following constraints: i) From W mass corrections at Next to Leading Order (NLO) [69]: For $250 \text{ GeV} \leq m_{h_2} \leq 850 \text{ GeV}$, one has $0.2 \leq \sin\beta \leq 0.3$. ii) For the requirement of perturbative unitarity [70]: $\sin\beta \leq 0.2$ for $m_{h_2} \geq 850 \text{ GeV}$. iii) Direct search measurement of Higgs signal strength at LHC provides an upper limit on mixing angle $|\sin\beta| < 0.36$ [70].

5.5 Relic abundance of dark matter

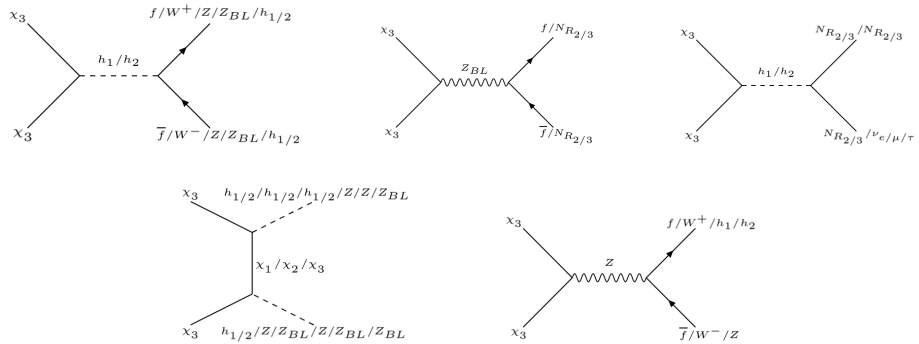


Figure 9: Additional annihilation channels of the DM (χ_3) to SM particles in $U(1)_{B-L}$ model.

The DM-SM interaction terms which deplete the number density of dark sector particles in the gauged $U(1)_{B-L}$ case has been discussed in Appendix B. The additional relevant Feynman diagrams of annihilation and coannihilation processes over and above those already present in section 3 are shown in Fig. 9, Fig. 10 and Fig. 11.

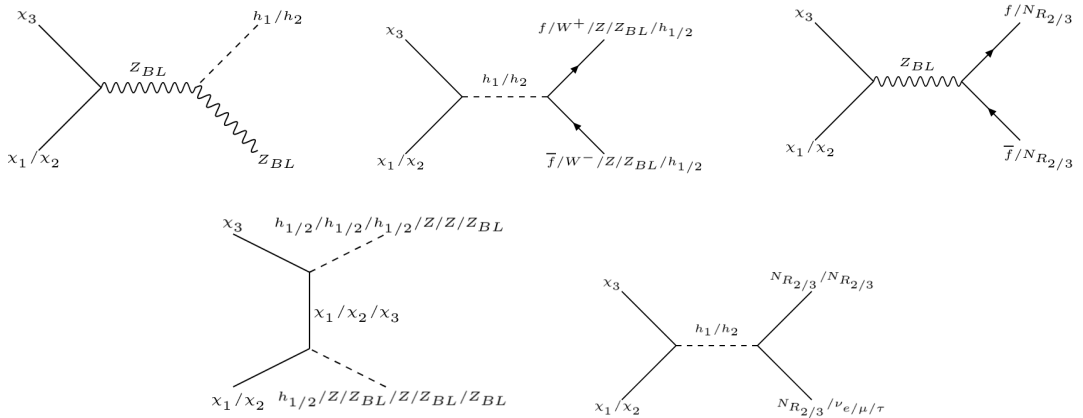


Figure 10: Additional coannihilation channels of DM (χ_3) with χ_1 , χ_2 and ψ^\pm in the $U(1)_{B-L}$ model.

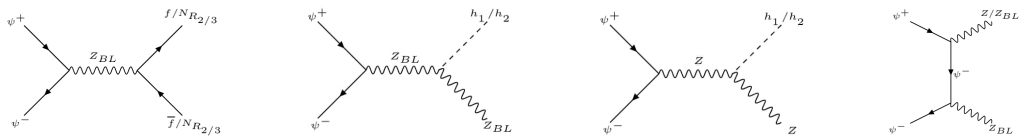


Figure 11: Additional coannihilation channels of ψ^+ and ψ^- that contribute to relic density of DM (χ_3) in the $U(1)_{B-L}$ model.

Again we use `MicrOmegas` to calculate the relic density of DM. The plots for DM relic density Ωh^2 as a function of DM mass $m_{DM} = m_{\chi_3}$ are shown in Fig. 12 for different mass splitting ΔM between the DM and the NLSP and for a chosen mixing angle $\sin \theta_{13}$. The main difference in this $B-L$ extended case compared to section 3 is the presence of new resonances at $m_{\chi_3} = m_{h_1}/2$ and $m_{\chi_3} = m_{h_2}/2$. These resonances get prominent only when the mass difference ΔM is sufficiently large such that the coannihilation processes are practically negligible. As we can see from Fig. 12, for small ΔM , the coannihilation through off-diagonal Z and W^\pm mediated interactions dominate. Apart from that in Fig. 12 we also see new resonances (in comparison to Fig. 4) occur at $m_{\chi_3} = m_Z/2$ and $m_{\chi_3} = M_{Z_{BL}}/2$. Note that the resonance at $m_{\chi_3} = m_Z/2$ is proportional to $\sin \theta_{13}$. As a result in the limit $\sin \theta_{13} \rightarrow 0$ and new particles, say h_2 and Z_{BL} heavy enough we get back to the same situation as in Fig. 4.

In Fig. 12, we have chosen $M_{Z_{BL}} = 1.65$ TeV, $g_{BL} = 0.03$, $m_{h_2} = 300$ GeV and the mixing parameter of SM Higgs with the new B-L Higgs as $\sin \beta = 0.2$, consistent with the available constraints. Also the masses of the two \mathcal{Z}_2 even right handed neutrinos are kept fixed as $M_{R_{2/3}} = 500$ GeV. As $\sin \theta_{13}$ increases, the Yukawa coupling between the doublet and the singlet increases, and hence the h_1 (SM-like Higgs) mediated interactions become more and more dominant. It is also clear from Fig. 12 that, irrespective of the mass difference ΔM , with increasing $\sin \theta_{13}$ the annihilation rates increase making deeper resonance drops. Due to the presence of off-diagonal interactions in all cases, all resonance drops has been somewhat

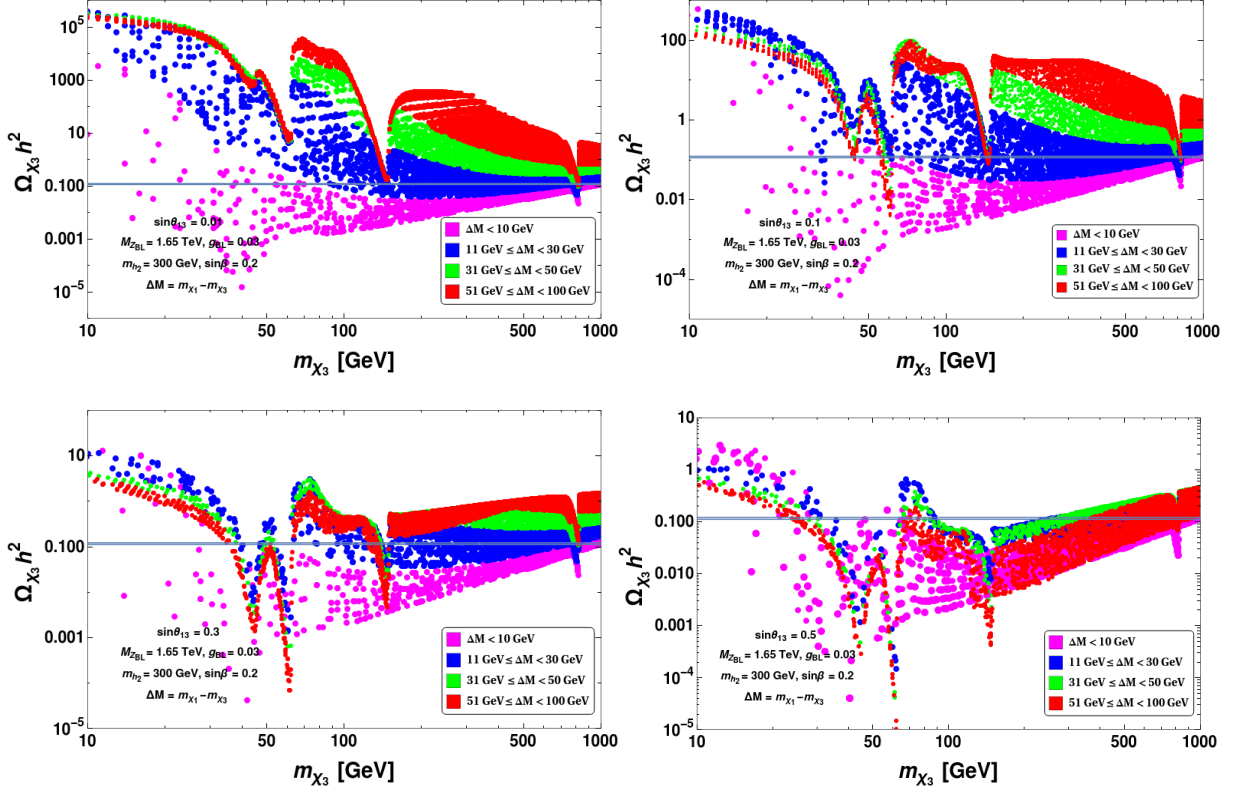


Figure 12: DM relic density as a function of DM mass (m_{χ_3}) for different mass splitting ΔM between the DM and the NLSP (shown by different coloured patches as indicated in figure inset) for fixed values of $\sin \theta_{13} = 0.01$ (top left panel), $\sin \theta_{13} = 0.1$ (top right panel), $\sin \theta_{13} = 0.3$ (bottom left panel) and $\sin \theta_{13} = 0.5$ (bottom right panel). Correct relic abundance from PLANCK data ($0.1166 \leq \Omega h^2 \leq 0.1206$) is shown by the thick horizontal silver line. The other parameters kept fixed are: $M_{Z_{BL}} = 1.65$ TeV, $g_{BL} = 0.03$, $m_{h_2} = 300$ GeV, $\sin \beta = 0.2$.

broadened up compared to the case of pure diagonal interactions.

In Fig. 13, the correct relic abundance is plotted in the plane of ΔM vs m_{χ_3} , where $\Delta M = (m_{\chi_1} - m_{\chi_3})$. Again, the main outcome remain almost similar as before, excepting the presence of additional peak at $m_{\chi_3} = \frac{M_{Z_{BL}}}{2}$ GeV due to Z_{BL} resonance. Other resonances at $m_Z/2, m_{h_1}/2, m_{h_2}/2$ are also visible. Just before the Z_{BL} resonance, we can see the effect of off-diagonal Z_{BL} mediated interactions (see B.3).

We note here that in the limit $\sin \theta_{23} \rightarrow 0$ (alongwith $g_{BL} \rightarrow 0, \sin \beta \rightarrow 0$ and for very heavy Z_{BL} and h_2), Fig. 13 reduces to Fig. 5, i.e. $U(1)_{B-L}$ extension boils down to the one without it.

5.6 Direct Detection prospects

The DM candidate (χ_3) in this model is a Majorana fermion, hence the Z and Z_{BL} -mediated vector current interaction vanishes. Although there is a possibility of spin dependent scattering through axial vector interaction mediated by the vector bosons, the sensitivity and bounds

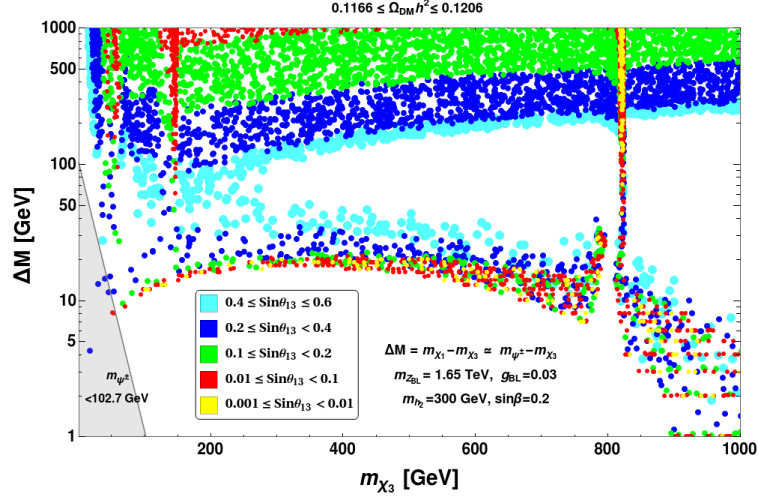


Figure 13: DM relic density ($0.1166 \leq \Omega_{DM} h^2 \leq 0.1206$) allowed parameter space shown in $\Delta M - m_{\chi_3}$ plane for the $U(1)_{B-L}$ model. Different coloured points indicate different ranges of $\sin \theta_{13}$ as specified in the figure inset. The parameters kept fixed for the scan are $M_{Z_{BL}} = 1.65$ TeV, $g_{BL} = 0.03$, $m_{h_2} = 300$ GeV, $\sin \beta = 0.2$. The shaded region in the bottom left corner is ruled out by LEP exclusion bound on charged fermion mass, $m_{\psi^\pm} = M > 102.7$ GeV.

are extremely weak. Therefore the prominent channel for direct detection of χ_3 is through $H - \Phi_{BL}$ mixing, which results in spin-independent scattering of DM off nuclei. The Feynman diagram for such interaction is shown in Fig. 14. The spin-independent DM-nucleon elastic scattering cross-section is again given by Eqn.-4.1. However, in contrast to the previous case, here there are two propagators (h_1 and h_2) that can mediate the DM pair production and hence direct detection is through the interference of two diagrams. So in this case the effective coupling strength α_q is given by:

$$\alpha_q = \frac{m_q}{v} \left(\frac{\lambda_a \cos \beta}{m_{h_1}^2} - \frac{\lambda_b \sin \beta}{m_{h_2}^2} \right), \quad (5.27)$$

where

$$\begin{aligned} \lambda_a &= \frac{Y_1}{2} (s_{13} + s_{23} c_{13}) c_{13} c_{23} \cos \beta - \frac{y'_1}{2\sqrt{2}} c_{13}^2 c_{23}^2 \sin \beta, \\ \lambda_b &= -\frac{Y_1}{2} (s_{13} + s_{23} c_{13}) c_{13} c_{23} \sin \beta - \frac{y'_1}{2\sqrt{2}} c_{13}^2 c_{23}^2 \cos \beta. \end{aligned} \quad (5.28)$$

In the numerical calculation we use the Yukawa coupling $Y_1 \approx \Delta M \sin 2\theta_{13}/v$ as given by Eqn. 5.23 and $y'_1 = \sqrt{2} M_{R_1}/v_{BL} = 2\sqrt{2} M_{R_1} g_{BL}/M_{Z_{BL}}$. So the direct search cross-section indirectly depends on ΔM , g_{BL} and $M_{Z_{BL}}$ as well.

The relative minus sign between the two propagators comes from the orthogonal mixing matrix in Eqn. 5.13. From Eqs. 4.1, 4.2, 4.3 and 5.27, the spin-independent scattering cross-section is given by,

$$\begin{aligned} \sigma^{SI} &= \frac{\mu_r^2}{\pi A^2} \left(\frac{\lambda_a \cos \beta}{m_{h_1}^2} - \frac{\lambda_b \sin \beta}{m_{h_2}^2} \right)^2 \left[Z \frac{m_p}{v} \left(f_{Tu}^p + f_{Td}^p + f_{Ts}^p + \frac{2}{9} f_{TG}^p \right) \right. \\ &\quad \left. + (A - Z) \frac{m_n}{v} \left(f_{Tu}^n + f_{Td}^n + f_{Ts}^n + \frac{2}{9} f_{TG}^n \right) \right]^2 \end{aligned} \quad (5.29)$$

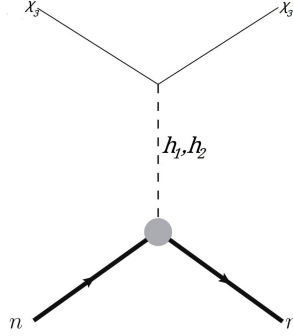


Figure 14: Feynman Diagram for elastic scattering of DM off nuclei at terrestrial laboratory in the $U(1)_{B-L}$ extended model.

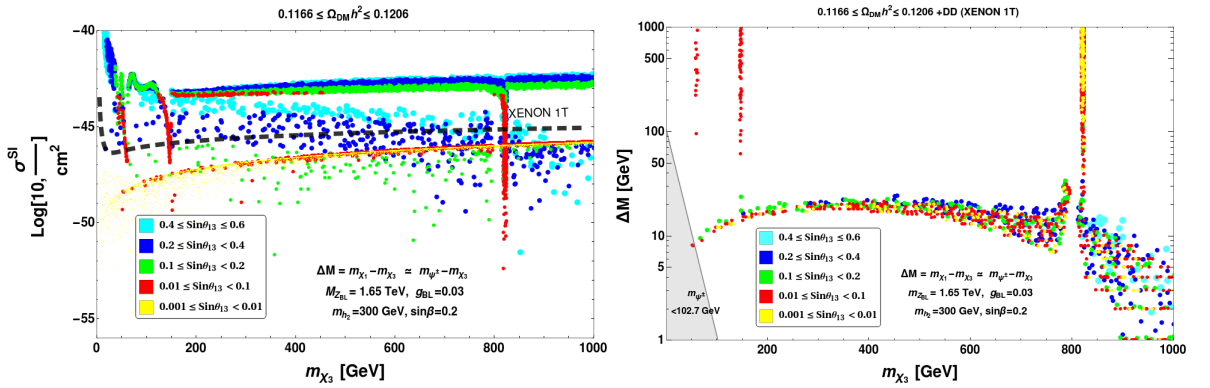


Figure 15: [Left]: Spin-independent direct detection cross section of DM (χ_3) with nucleon as function of DM mass (in GeV) for $U(1)_{B-L}$ model confronted with XENON-1T data over and above relic density constraint from PLANCK; [Right]: Correct DM relic density allowed parameter space of the model in $\Delta M - m_{\chi_3}$ plane constrained by XENON-1T bound. Different coloured points indicate different ranges of $\sin \theta_{13}$ as mentioned in the figure inset. The parameters kept fixed for the scan are $M_{Z_{BL}} = 1.65$ TeV, $g_{BL} = 0.03$, $m_{h_2} = 300$ GeV, $\sin \beta = 0.2$. The shaded region in the bottom left corner of right hand plot is ruled out by LEP exclusion bound on charged fermion mass, $m_{\psi^\pm} = M > 102.7$ GeV.

Now we turn to the parameter space of the model consistent with direct search constraints. In left panel of Fig. 15, we have confronted the points satisfying relic density with the spin independent elastic cross section obtained for the model as a function of DM mass. The XENON-1T bound is shown by dashed black line. Again, the region below this line satisfy both relic density as well as direct detection constraint. These points (satisfying relic density as well as direct detection constraint from XENON-1T) are shown in the right panel of Fig. 13 in the $\Delta M - m_{\chi_3}$ plane. Again we see that null observation from direct search crucially tames down the relic density allowed parameter space. The available parameter space of the $U(1)_{B-L}$ model is very similar to that without the gauge extension, excepting for the resonance regions at $m_{\chi_3} = m_{h_{1/2}}/2$ and $m_{\chi_3} = M_{Z_{BL}}/2$, where ΔM can be uncorrelated to DM mass.

5.7 ATLAS bound on $g_{BL} - M_{Z_{BL}}$

We now turn to find the allowed parameter space in the $\Delta M - m_{\chi_3}$ plane in light of ATLAS bound on g_{BL} versus $M_{Z_{BL}}$. In the previous sections we kept $M_{Z_{BL}}$ fixed at 1650 GeV corresponding to $g_{BL} = 0.03$ compatible with ATLAS data [65]. As a result of choosing such a small value of g_{BL} , the effect of Z_{BL} was only evident at resonance when $m_{\chi_3} \sim M_{Z_{BL}}/2$ (see Fig. 15). In the following we highlight the effect of Z_{BL} mediated diagrams by varying the coupling and mass. We perform a scan by varying the model parameters in the following range:

$$\left\{ \begin{array}{l} 1 \text{ GeV} \leq m_{\chi_3} \leq 2000 \text{ GeV} \\ 1 \text{ GeV} \leq \Delta M \leq 1000 \text{ GeV} \\ 20 \text{ GeV} \leq M_{Z_{BL}} \leq 4000 \text{ GeV} \\ 0.001 \leq \sin \theta_{13} \leq 0.6 \\ 0.001 \leq g_{BL} \leq 0.3. \end{array} \right. \quad (5.30)$$

Other parameters kept fixed are: $\sin \beta = 0.2$ and $m_{h_2} = 300$ GeV. Also the masses of the two \mathcal{Z}_2 even right handed neutrinos are kept fixed as $M_{R_{2/3}} = 500$ GeV.

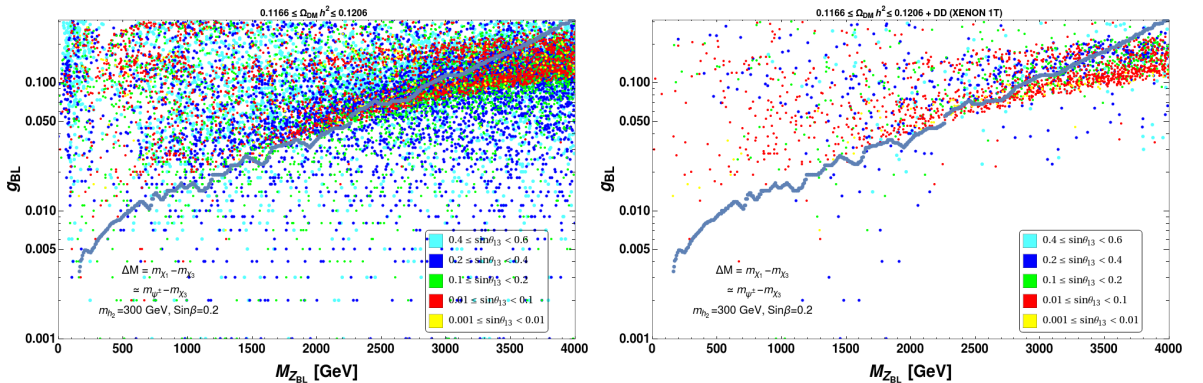


Figure 16: [Left]: Parameter space satisfying relic density constraint from PLANCK ($0.1166 \leq \Omega_{DM} h^2 \leq 0.1206$) in the plane of $g_{BL} - M_{Z_{BL}}$ for $U(1)_{B-L}$ model; [Right]: Parameter space satisfying both relic density constraint from PLANCK and direct detection bound from XENON-1T in the plane of $g_{BL} - M_{Z_{BL}}$. The thick silver line shows the ATLAS bound on g_{BL} vs $M_{Z_{BL}}$ [65] plane from non-observation of Z_{BL} in collider data.

We first show the constraint coming from non-observation of a new gauge boson (Z_{BL}) at LHC coming from ATLAS [65] analysis on g_{BL} for corresponding values of $M_{Z_{BL}}$ shown by the silver thick line in Fig. 16. This indicates that points below the line with smaller g_{BL} is allowed, while those above the line are discarded. The left plot shows points which satisfy relic density constraint from PLANCK ($0.1166 \leq \Omega_{DM} h^2 \leq 0.1206$) data and right plot shows the points which satisfy both relic density and direct search bounds from XENON 1T. Different colours indicate ranges of $\sin \theta_{13}$ as mentioned in figure inset. We then showcase the fate of the model when the bound from ATLAS is implemented on the parameter space in ΔM vs m_{χ_3} plane for different g_{BL} values in Fig. 17. In the top panel we show the available parameter

space in terms of different ranges of $\sin\theta_{13}$, while the same is shown in bottom panel for different ranges of g_{BL} coupling for relic density and direct search allowed parameter space of the $U(1)_{B-L}$ model. For clarity in inferring how much parameter space gets discarded by the ATLAS bound, in the left panel we show relic density and direct search allowed points without ATLAS bound, while on the right panel, we show those after incorporating ATLAS bound [65].

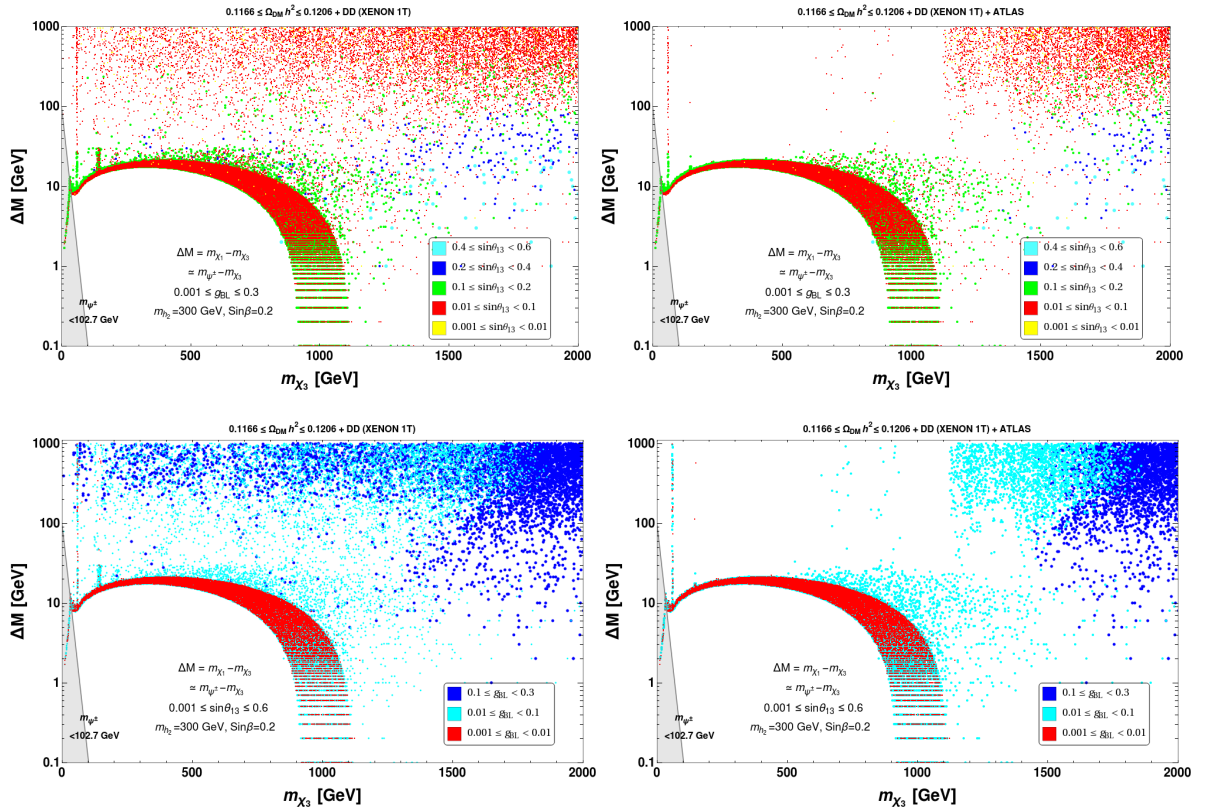


Figure 17: [Top Left]: Parameter space satisfying relic density (PLANCK) and direct search (XENON-1T) bound in $\Delta M - m_{\chi_3}$ plane, different colours indicate different choices of $\sin\theta_{13}$; [Top Right]: Same as top left but additionally ATLAS bound on $g_{BL} - M_{Z_{BL}}$ [65] applied; [Bottom Panel]: Same as in the top panel, but different coloured points indicate different ranges of g_{BL} coupling as mentioned in figure inset, with left (right) plot without respecting (with) ATLAS bound. The shaded region in the bottom left corner is ruled out by LEP exclusion bound on charged fermion mass, $m_{\psi^\pm} = M > 102.7$ GeV.

We see from Fig. 17 when $\Delta M \lesssim 10$ GeV, the contribution to relic density comes from annihilation, coannihilation and Z_{BL} resonance with relatively smaller g_{BL} . As we go for further larger ΔM , the coannihilation contribution to relic density decreases gradually and gets compensated by Z_{BL} exchange diagrams with increasing values of g_{BL} . Beyond $m_{\chi_3} = 1000$ GeV, the correlation between ΔM and m_{χ_3} is lost and relic is mostly dominated by Higgs and Z_{BL} mediation. In the right panel of Fig. 17, we impose bound on $g_{BL} - M_{Z_{BL}}$ from ATLAS data. The upper bound on g_{BL} by ATLAS data for lighter Z_{BL} is extremely small (for e.g., $M_{Z_{BL}} \sim O(1\text{TeV})$, upper bound on $g_{BL} \sim 0.009$ [68]). Consequently if we have to satisfy

ATLAS bound, then all those resonance points with large g_{BL} in the left panel of Fig. 17 upto $m_{\chi_3} \sim 500$ GeV are no longer there in the right panel of Fig. 17. It is only when $M_{Z_{BL}}$ becomes sufficiently large, so that g_{BL} can take somewhat moderate values, we can see the Z_{BL} resonance affects. That is why in the right panel of Fig. 17, such resonance points survive for $m_{\chi_3} \geq 500$ GeV. For $m_{\chi_3} > 1000$ GeV, the points which survive the ATLAS bound are mostly due to Z_{BL} resonances with relatively large g_{BL} . Note that the direct detection cross section has mild dependency on these resonance points. Therefore, these resonance points for $m_{\chi_3} > 1000$ GeV also easily survive from XENON-1T bound.

6 Collider Signatures

Both the model frameworks studied here, have attractive signatures at the Large Hadron Collider (LHC) due to the presence of SM isodoublet. There exists different types of production processes and decay final states which can be categorized broadly into leptonic and hadronic final states. Leptonic final states are favoured over hadronic states for less SM contamination. All the heavier dark sector particles finally decay into the DM (χ_3), which is missed in the detector and necessarily associate each final state with missing transverse energy (E_T) defined as:

$$\cancel{E}_T = -\sqrt{\left(\sum_{\ell,j,unc} p_x\right)^2 + \left(\sum_{\ell,j,unc} p_y\right)^2}, \quad (6.1)$$

where the sum runs over all visible objects that include leptons ($\ell = e, \mu$) and jets, and unclustered components. Here we list some of the most important leptonic final states that the models offer. We will refer to the model without $U(1)_{B-L}$ as model I and the one with $U(1)_{B-L}$ extension as model II.

- Opposite sign dilepton ($\ell^+\ell^- + E_T$):

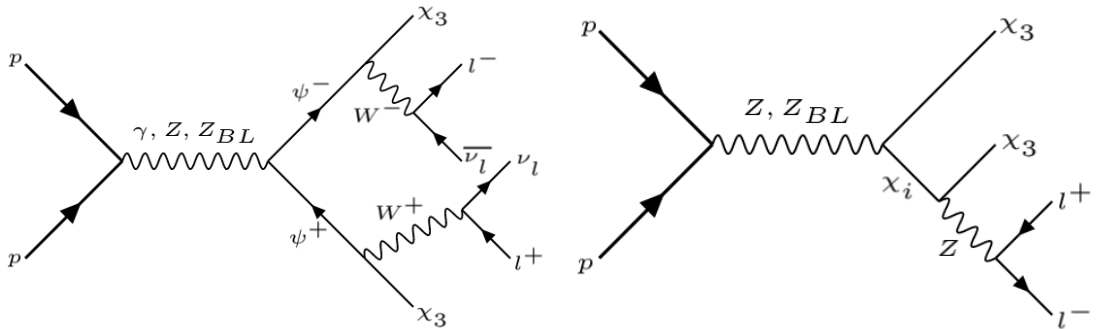


Figure 18: OSD + E_T signal at LHC due to: (i) (Left) $\psi^+ \psi^-$ production and (ii) (Right) $\chi_3 \chi_i$ production. For model II $i = 1, 2$, for model I, $i = 2$.

The heavy charged component of $SU(2)_L$ doublet, ψ^\pm (NLSP) can be produced via (Z, γ) mediation in model I and (Z, γ, Z_{BL}) mediation in model II. Further they decay to leptonic final state via on-shell or off-shell W^\pm mediator (depending on mass splitting $m_{\psi^\pm} - m_{\chi_3}$) and stable DM (χ_3). As a result the process yields hadronically quiet opposite sign dilepton (OSD) plus missing energy ($\ell^+\ell^- + E_T$) signature at collider as shown in the Feynman graph in the left panel of Fig. 18:

$$OSD + E_T : p p \rightarrow \psi^+ \psi^-, (\psi^- \rightarrow \ell^- \bar{\nu}_\ell \chi_3), (\psi^+ \rightarrow \ell^+ \nu_\ell \chi_3); \ell = \{e, \mu\}.$$

Also the production of $\chi_i \chi_3$ pair via Z propagator in model I and Z, Z_{BL} propagator in model II gives rise to OSD final state as shown in right panel of Fig. 18:

$$OSD + E_T : p p \rightarrow \chi_i \chi_3 (\chi_{1,2} \rightarrow \ell^- \ell^+ \chi_3); \ell = \{e, \mu\} \quad i = \{1, 2\}.$$

It is important to note that in model I, $i = 2$ is the only possibility [see appendix A and Eq. A.2 in particular]. Also note that the production of the heavy neutral components as above are proportional to the mixing angle ($\sin\theta$), which is small (to respect direct search constraints). Therefore $\chi_i \chi_3$ production is suppressed than the $\psi^+ \psi^-$ production process, which is independent of mixing angle ($\sin\theta$).

It is worth mentioning that similar process have been studied widely in context of supersymmetric theories by chargino pair production at LHC [71–80]. Non observation of any excess in OSD signal events at LHC results in a bound on the charged fermion mass. The bound(s) obtained for charginos are often specific to supersymmetric model given so many additional parameters that the theory inherits and may not be applicable (fully) to our case. Recasting the full analysis in our case is also out of the scope of this draft and will be taken up elsewhere. We will however provide a short account of the event simulation procedure and hint towards some broad conclusions. Note however that a model independent bound was found in context of LEP experiment as $m_{\psi^\pm} \gtrsim 102.7$ GeV [81]. One may also look into [40, 45] for event level analysis at LHC without $U(1)_{B-L}$ case and in [82] for $U(1)_{B-L}$ case.

- Three leptons ($\ell\ell\ell + E_T$):

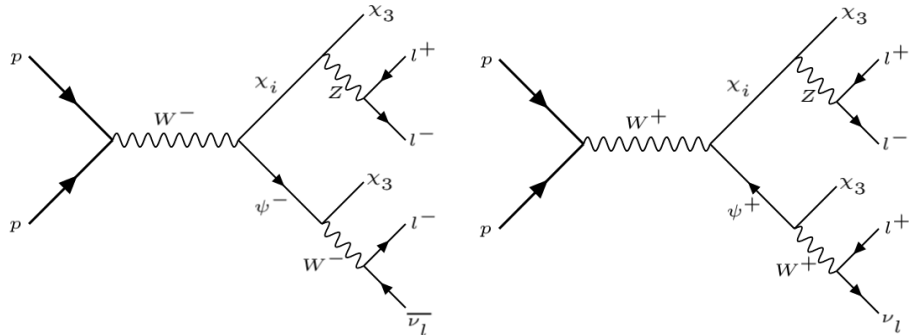


Figure 19: $\ell\ell\ell + E_T$ signal at LHC. For model I, $i = \{1, 2\}$, while for model II, $i = 2$.

Hadronically quiet trilepton plus missing energy signature can be obtained from the production of heavy neutral, $\chi_{1,2}$ and charged fermions states, ψ^\pm via W^\pm mediator as shown in Fig. 19:

$$3\ell + E_T : p p \rightarrow \psi^\pm \chi_i, (\psi^\pm \rightarrow \ell^\pm \nu_\ell(\bar{\nu}_\ell) \chi_3), (\chi_i \rightarrow \ell^- \ell^+ \chi_3); \ell = \{e, \mu\} \quad i = \{1, 2\} .$$

Again, it is worth noting that although the production process is same in both model I and model II, subsequent decay of $\chi_i \rightarrow \chi_3 Z^*$ is only allowed for χ_2 in model I and provides a way of distinguishing the two cases. The fact that no significant excess in hadronically quiet trilepton events are observed at LHC and the result agrees to SM contribution to a great extent puts a bound on the relevant parameters. From ATLAS data, following constraints can be obtained: $m_{\chi_{1,2}}, m_{\psi^\pm} < 270$ GeV, $m_{\chi_3} \lesssim 70$ GeV with BR ($\chi_{1,2} \rightarrow Z\chi_3$) $\gtrsim 60\%$ [83]. We may note that similar trilepton signature can also arise from Higgsino-Bino production in supersymmetric models, which have been studied in context of LHC data [72].

- Four leptons ($\ell\ell\ell\ell + E_T$):

The heavy neutral fermionic DM states, $\chi_{1,2}$ (NLSP) can be produced at LHC via Z propagator in model I and Z, Z_{BL} propagator in model II. The heavy states, $\chi_{1,2}$ further decay to leptonic final states via Z and produce four leptons plus missing energy signature as shown in Fig. 20:

$$\ell\ell\ell\ell + E_T : p p \rightarrow \chi_i \chi_j, (\chi_{i,j} \rightarrow \ell^- \ell^+ \chi_3); \ell = \{e, \mu\}; \quad i, j = \{1, 2\} .$$

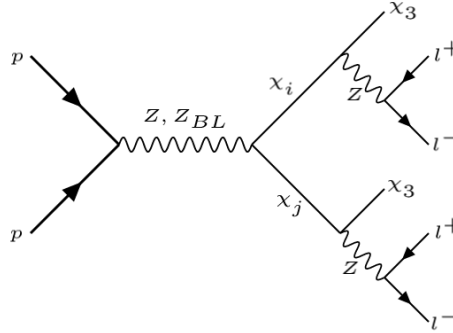


Figure 20: $\ell\ell\ell\ell + E_T$ signal in model II at LHC ($i, j = \{1, 2\}, i \neq j$).

We should note here that there are two main issues of producing four lepton states: (i) We need to produce $\chi_1\chi_2$ pair, (ii) then $\chi_{1,2}$ both needs to decay via Z to χ_3 . Now from interaction vertex in appendix A and Eq. A.2, we see that the decay of χ_1 can't occur to $\chi_3 Z^*$ unless the model is extended by $U(1)_{B-L}$ [see appendix B and Eq. B.2], thus making the signal exclusive for the $U(1)_{B-L}$ extension. Apart, one may also have hadronically quiet six lepton states arising from the decay of $\chi_1 \rightarrow \chi_2 Z^*, \chi_2 \rightarrow \chi_3 Z^*$, followed by leptonic decays of the off-shell Z from the same production process for both models with $U(1)_{B-L}$ extension and without that.

- Single lepton with jets ($\ell^\pm + jj + E_T$):

The leptons in the final state arise out of W and Z boson decays (see Figs. 18, 19, 20), which anyway could also decay to quark antiquark pair to yield jets. Therefore, apart from purely leptonic signatures, one may also have hadrons or jet-rich final states. For example, the charged fermion pair production can lead to single lepton with two jets plus missing energy signature when one off shell W decays to hadronic final state (see Fig. 18). Obviously when both W decays hadronically, one ends up with four (or more) jets. LHC being a QCD machine, hadronic final states are prone to huge SM QCD background and therefore disfavoured. In event analysis, segregating signal from SM background is an important task. Missing energy variable as introduced in Eq. 6.1 play a crucial role, as in SM contributions to E_T mainly arise from neutrinos and mistagging.

- Displaced vertex signature of ψ^\pm :

We already observed that a large region of available parameter space of the model relies on small ΔM (for example, see in the right panel of Fig. 8). The decay of ψ^\pm is then phase space suppressed and can produce a displaced vertex, which can serve as a very crucial signature of the model. The decay length in its rest frame (following from Eq. 3.6) is given by,

$$L_0 = \frac{1.9 \times 10^{-2} \text{ cm}}{\left(\frac{\Delta M}{\text{GeV}}\right)^5 \sin \theta}.$$

In Fig. 21, we show the decay length of ψ^\pm as a function of ΔM for fixed $\sin \theta$ values depicted in different colours. We see that for $\Delta M < 10$ GeV, the displaced vertex of ψ^\pm can be significantly large to be detected at the collider. On the other hand, non-observation of a displaced vertex or a charge track will result in a bound on $\Delta M - \sin \theta$ plane.

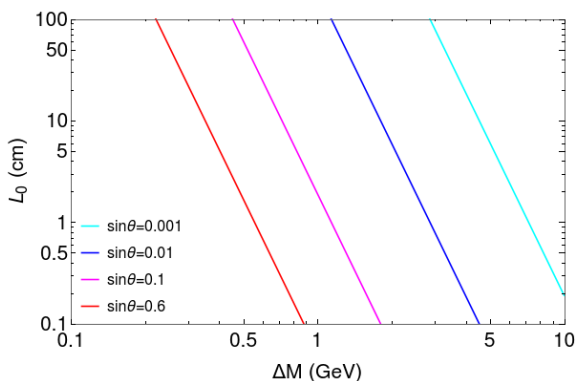


Figure 21: The decay length of ψ^\pm as a function of mass difference ΔM for fixed $\sin \theta$ values.

- Effect of $B - L$ gauge extension in $\psi^+\psi^-$ pair production:

The effect of $U(1)_{B-L}$ gauge boson (Z_{BL}) mediation in $pp \rightarrow \psi^+\psi^-$ production [84] is an important question and we discuss the main features here. We summarise our obser-

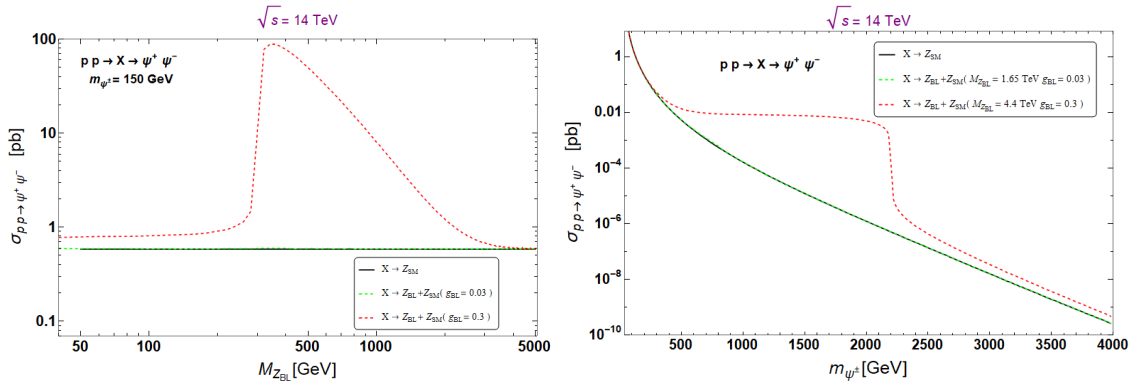


Figure 22: [Left] The production cross-section of $\psi^+\psi^-$ pairs at collider is shown as a function of $U(1)_{B-L}$ gauge boson mass, $M_{Z_{BL}}$ for fixed $m_{\psi^\pm} = 150$ GeV. Different coloured lines depict different cases: SM production cross-section is shown by black solid line; $U(1)_{B-L}$ case is shown for $g_{BL} = 0.03$ (green dashed line) and $g_{BL} = 0.3$ (red dashed line). [Right] The production cross-section of $\psi^+\psi^-$ pairs at collider is shown as a function of m_{ψ^\pm} with $M_{Z_{BL}} = 1.65$ TeV, $g_{BL} = 0.03$ (green dashed line) and $M_{Z_{BL}} = 4.4$ TeV, $g_{BL} = 0.3$ (red dashed line). Pure SM gauge boson mediated production cross-section (Model I) is also shown in black solid line.

vations in Fig. 22. In the left panel of Fig. 22, we have shown the production cross-section of $\psi^+\psi^-$ pair at LHC as a function of $M_{Z_{BL}}$ for fixed $m_{\psi^\pm} = 150$ GeV. On the right panel, we plot the production cross-section of $\psi^+\psi^-$ as function of m_{ψ^\pm} , for two different combinations of Z_{BL} parameters: $\{M_{Z_{BL}} = 1.65$ TeV, $g_{BL} = 0.03\}$ (green dashed line) and $\{M_{Z_{BL}} = 4.4$ TeV, $g_{BL} = 0.3\}$ (red dashed line), which agree to the current ATLAS bound. Only SM contribution with $Z_{SM} : (Z, \gamma)$ mediation is also shown by black solid line for comparison. It is evident from the Fig. 22, that for the smaller value $g_{BL} = 0.03$, the contribution from Z_{BL} mediated production is negligible compared to SM and consequently green dashed and black lines fall on top of each other. However, with a moderate value of $g_{BL} = 0.3$, the production cross-section significantly improves with Z_{BL} mediation, which is seen in red dashed line clearly separated from the other two. In the left plot we see that the effect of s-channel resonance in amplitude $\sim \frac{1}{\hat{s} - M_{Z_{BL}}^2}$ showing up at $M_{Z_{BL}} = 2m_{\psi^\pm} = 300$ GeV as the minimum subprocess center-of-mass energy required for this process to occur is $\sqrt{\hat{s}} = 300$ GeV with $m_{\psi^\pm} = 150$ GeV. The resonance is extended to account its finite decay width $\sim \frac{1}{\hat{s} - M_{Z_{BL}}^2 + iM_{Z_{BL}}\Gamma_{Z_{BL}}}$. The same effect is seen on the right panel plot where the resonance rise is visible at $m_{\psi^\pm} = \frac{M_{Z_{BL}}}{2} \sim 2$ TeV for the red dashed curve ($g_{BL} = 0.3$). To summarise, the effect of Z_{BL} mediation for the production of ψ^\pm pair, which contributes to opposite sign dilepton (OSD) plus missing energy signal, can only be realised at relatively larger values of gauge coupling (g_{BL}) and on-shell Z_{BL} production whenever possible, albeit that current experimental bound requires a higher Z_{BL} mass with larger g_{BL} coupling (see Fig. 16).

- Hadronically quiet OSD events at LHC:

We shall now briefly discuss the event level simulation for the OSD signal ($\ell^+\ell^- + \cancel{E}_T$) and estimate SM background contamination for the same final state. Our elaboration will be more indicative than exhaustive. For that, we refer to two different benchmark points with $\Delta M = 15$ GeV and 300 GeV keeping DM mass fixed at $m_{\chi_3} = 150$ GeV; important to note here that the first case applies to the model I without $B - L$ extension where the second possibility with larger ΔM is only allowed in model II with $B - L$ extension (compare Fig. 8 to Fig. 17). For the analysis we generate the `lhe` file from the model implementation in `FeynRule` [57] and run it in `Madgraph` [85] to generate events and finally pass onto `Pythia` [86] for analysis. Following basic techniques are used in `Pythia` to mimic the actual collider environment:

- **Lepton isolation:** To identify a lepton ($\ell = e, \mu$) in the detector, one requires a minimum transverse momentum, which we keep as $p_T > 20$ GeV. We also require the pseudorapidity within $|\eta| < 2.5$, which ensures that leptons ejected centrally can only be observed in the detector. Separation of leptons from each other requires $(\Delta R)_{\ell\ell} \geq 0.2$ in $\eta - \phi$ plane (where $\Delta R = \sqrt{(\Delta\eta)^2 + (\Delta\phi)^2}$). We further imposed $(\Delta R)_{\ell j} \geq 0.4$ to separate leptons from jets.
- **Jet identification:** Defining a jet (j) is an important issue at LHC environment. In the numerical simulation performed here, jets are formed in `Pythia` using cone algorithm inbuilt in `PYCELL`. A jet is then identified with all parton within a cone of $\Delta R \leq 0.4$ around a jet initiator with $p_T > 20$ GeV. We will finally require zero jet veto to ensure hadronically quiet final state.
- **Unclustered objects:** The unclustered objects consist of those objects, which neither qualify as jets nor identified as isolated leptons (following our previous definitions) and only contribute to missing energy. All final state objects with smaller transverse momentum $0.5 < p_T < 20$ GeV and larger pseudorapidity $2.5 < |\eta| < 5$ are therefore identified as unclustered objects.

Three kinematic variables play a key role in the analysis: Missing Energy (\cancel{E}_T), Transverse Mass (H_T) and Invariant mass ($m_{\ell\ell}$); where the signal and background show different sensitivity. Missing energy has already been defined (Eq. 6.1), the other two are:

- Transverse Mass (H_T): Transverse mass of an event is identified to:

$$H_T = \sum_{\ell, j} \sqrt{(p_x)^2 + (p_y)^2} = \sum_{\ell, j} p_T, \quad (6.2)$$

where the *scalar sum* of transverse momentum runs over reconstructed objects like leptons (ℓ) and jets (j).

- Invariant mass ($m_{\ell\ell}$): Invariant mass of opposite sign dilepton is defined by

$$m_{\ell^+\ell^-} = \sqrt{\left(\sum_{\ell^+\ell^-} p_x\right)^2 + \left(\sum_{\ell^+\ell^-} p_y\right)^2 + \left(\sum_{\ell^+\ell^-} p_z\right)^2}. \quad (6.3)$$

The normalised event distribution for OSD signal events $\ell^+\ell^- + (\cancel{E}_T)$ at the two benchmark points with dominant SM background events are shown in Fig. 23 with missing energy

(\cancel{E}_T) in the left panel and transverse mass (H_T) on the right panel. In both graphs, we note that the peak for $\Delta M = 15$ GeV appear on the left side of SM background, while the one for $\Delta M = 300$ GeV is flatter and shifted towards high \cancel{E}_T/H_T value. It is then quite apparent, that segregating these two signals from SM background requires different selection cuts on \cancel{E}_T , H_T and $m_{\ell\ell}$, which are chosen as follows:

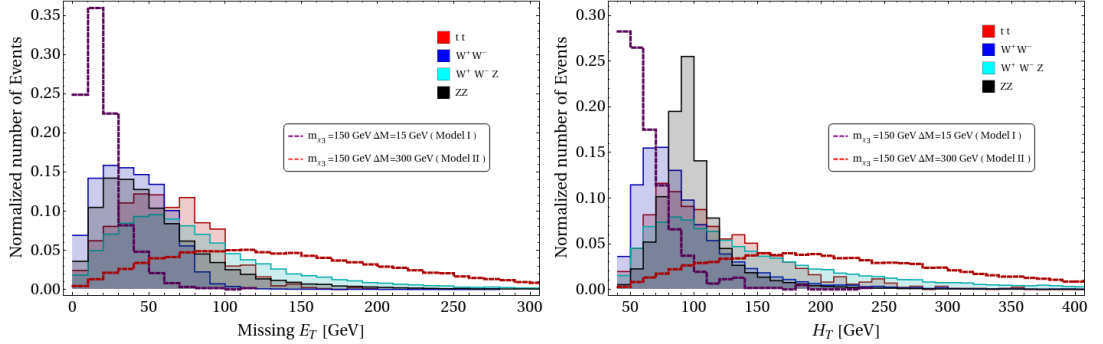


Figure 23: Distribution of missing energy (\cancel{E}_T) and transverse mass (H_T) for signal events and dominant SM background events at LHC with $\sqrt{s} = 14$ TeV .

- Invariant mass ($m_{\ell\ell}$) cut: $m_{\ell\ell} < (m_Z - 15)$ GeV and $m_{\ell\ell} > (m_Z + 15)$ GeV is imposed to get rid of SM Z boson contribution to OSD final state.
- \cancel{E}_T and H_T cuts:
 - $\cancel{E}_T < 30$ GeV, $H_T < 70$ for $\Delta M = 15\text{GeV} < m_{W^\pm}$.
 - $\cancel{E}_T > 100$ GeV, $H_T > 150$ for $\Delta M = 300\text{GeV} > m_{W^\pm}$.

Model	m_{χ_3} (GeV)	ΔM (GeV)	$\sigma^{\ell^+\ell^-X}$ (fb)	\cancel{E}_T (GeV)	H_T (GeV)	$\sigma_{\text{eff}}^{\ell^+\ell^-X}$ (fb)	$N_{\text{eff}}^{\ell^+\ell^-X} (@\mathcal{L} = 10^2\text{fb}^{-1})$
Model I	150	15	392.37	< 30	< 70	1.48	148
Model II	150	300	9.48	> 100	> 150	1.83	183

Table 3: Signal ($\ell^+\ell^- + (\cancel{E}_T)$) cross-section for the chosen benchmark points for $\sqrt{s} = 14$ TeV at LHC with luminosity $\mathcal{L} = 100 \text{ fb}^{-1}$ in Model I (without $B - L$) and Model II (with $B - L$) after the selection cuts employed.

After imposing above cut-flow we list the signal and dominant SM background events in Table 3 and Table 4 respectively for luminosity 100 fb^{-1} . We see that W^+W^- production provides the most significant background for OSD at LHC, which couldn't be tamed by the cuts used. This is surely the key reason for not being able to observe any signal excess over the huge SM background at LHC. The numbers of signal and SM background events thus obtained can provide the discovery reach of the signal for two benchmark points in terms of significance defined as $\sigma = \frac{S}{\sqrt{S+B}}$, where S denotes signal events and B denotes SM background events,

SM Bkg.	$\sigma^{\ell^+\ell^-X}$ (fb)	\cancel{E}_T (GeV)	H_T (GeV)	$\sigma_{\text{eff}}^{\ell^+\ell^-X}$ (fb)	$N_{\text{eff}}^{\ell^+\ell^-X} (@\mathcal{L} = 10^2 \text{fb}^{-1})$
$t \bar{t}$	36.69×10^3	< 30	< 70	6.23	623
		> 100	> 150	10.64	1064
$W^+ W^-$	4.74×10^3	< 30	< 70	131.18	13118
		> 100	> 150	7.72	772
$Z Z$	0.25×10^3	< 30	< 70	0.53	53
		> 100	> 150	0.18	18
$W^+ W^- Z$	1.00	< 30	< 70	0.01	1
		> 100	> 150	0.06	6

Table 4: Dominant SM background contribution to $\ell^+\ell^- + (\cancel{E}_T)$ signal events for $\sqrt{s} = 14$ TeV at LHC for luminosity $\mathcal{L} = 100 \text{ fb}^{-1}$. The SM background cross-section are quoted with next-to-leading order (NLO) level with appropriate K-factors [87].

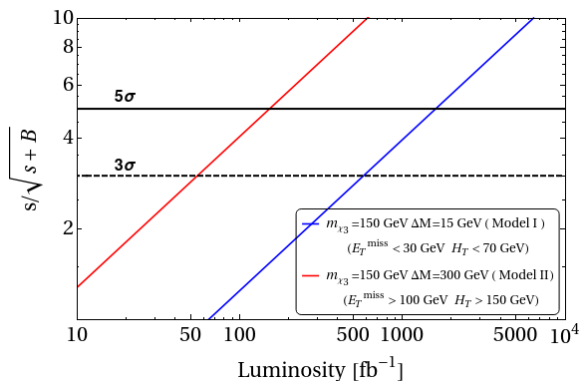


Figure 24: Signal significance $\sigma = \frac{S}{\sqrt{S+B}}$ of the benchmark points characteristic to model I (in blue) and model II (in red) at LHC with $\sqrt{s} = 14$ TeV, in terms of luminosity (fb^{-1}), subject to the selection criteria imposed in this analysis. 3σ and 5σ reach

shown as a function of luminosity in Fig. 24. It shows that 5σ discovery reach is difficult to achieve for the model I without $U(1)_{B-L}$ characterised by low ΔM ($\mathcal{L} \sim 1500 \text{ fb}^{-1}$), while the case with large ΔM in model II with $U(1)_{B-L}$ extension can be probed in near future with $\mathcal{L} \sim 150 \text{ fb}^{-1}$.

7 Non-zero masses and mixing of light neutrinos

The very construct of this model is motivated by the fact that we wish to have phenomenologically viable WIMP like DM and non-zero masses and mixing of light neutrinos in a minimal extension of the SM. This could be achieved by the presence of three RH neutrinos. While, one of them constitute the dark sector being odd under a stabilising \mathcal{Z}_2 symmetry, the other two can contribute to neutrino sector. In this model, a tiny yet non-zero neutrino mass can

be generated via Type I seesaw from the following terms in the Lagrangian 2.1,

$$-\mathcal{L}_{mass}^\nu \supset \left(Y_{j\alpha} \overline{N_{R_j}} \tilde{H}^\dagger L_\alpha + h.c. \right) + \left(\frac{1}{2} M_{R_j} \overline{N_{R_j}} (N_{R_j})^c + h.c. \right); \quad (7.1)$$

where $\alpha = e, \mu, \tau$ and $j = 2, 3$. After EW symmetry breaking, the SM Higgs acquires a vev to generate the Dirac mass terms for the neutrinos. In the gauged B-L scenario, the mass of all three right handed neutrinos are generated through the vev of the scalar Φ_{BL} . So for simplicity we can consider the mass of two \mathcal{Z}_2 even right handed neutrinos that take part in the seesaw to be quasi-degenerate and of the same mass scale as that of the \mathcal{Z}_2 odd right handed neutrino taking part in the dark sector phenomenology. Without loss of generality, we assume the heavy Majorana mass matrix that take part in seesaw to be diagonal, *i.e.*, $M_R = \text{Diag}(0, M_{R_2}, M_{R_3})$. In this basis, the light neutrino mass matrix obtained through Type-I seesaw is given as,

$$m_\nu = -m_D M_R^{-1} m_D^T \quad (7.2)$$

which is a complex 3×3 matrix and can be diagonalized by the PMNS matrix [88] as,

$$(m_\nu)^{diag} = U^T m_\nu U \quad (7.3)$$

where $(m_\nu)^{diag} = \text{Diag}(m_1, m_2, m_3)$ contains at least one zero eigenvalue.

The PMNS matrix U is given by:

$$U = \begin{pmatrix} c_{12}c_{13} & s_{12}c_{13} & s_{13}e^{-i\delta} \\ -s_{12}c_{23} - c_{12}s_{23}s_{13}e^{i\delta} & c_{12}c_{23} - s_{12}s_{23}s_{13}e^{i\delta} & s_{23}c_{13} \\ s_{12}s_{23} - c_{12}c_{23}s_{13}e^{i\delta} & -c_{12}s_{23} - s_{12}c_{23}s_{13}e^{i\delta} & c_{23}c_{13} \end{pmatrix} U_{ph} \quad (7.4)$$

where c_{ij} and s_{ij} stand for $\cos \theta_{ij}$ and $\sin \theta_{ij}$ respectively and U_{ph} is given by:

$$U_{ph} = \text{Diag}(1, e^{-i\alpha/2}, 1) \quad (7.5)$$

where α is the CP-violating Majorana phase.

Using Casas-Ibarra parameterization [89], the Dirac mass matrix m_D can be parametrized as,

$$(m_D)_{j\alpha} = \sqrt{M_{R_j}} R_{ji} \sqrt{m_i} U_{i\alpha}^\dagger \quad (7.6)$$

where m_i are the eigenvalues of the light neutrino mass matrix m_ν and R is in general a 3×3 complex orthogonal matrix. Since in our case, N_{R_1} is decoupled from the spectrum, the corresponding Yukawa coupling $Y_{1\alpha}$ for a particular flavour α in the Dirac mass matrix given by Eqn. 7.6 is zero, *i.e.*,

$$\begin{aligned} Y_{1\alpha} &= \frac{1}{v} (\sqrt{M_{R_1}} R_{1i} \sqrt{m_i} U_{i\alpha}^\dagger) \\ &= \frac{1}{v} (\sqrt{M_{R_1}} R_{11} \sqrt{m_1} U_{1\alpha}^\dagger + \sqrt{M_{R_1}} R_{12} \sqrt{m_2} U_{2\alpha}^\dagger + \sqrt{M_{R_1}} R_{13} \sqrt{m_3} U_{3\alpha}^\dagger) = 0 \end{aligned} \quad (7.7)$$

At present, the oscillation experiments measure two mass square differences: namely solar (Δm_{\odot}^2) and atmospheric (Δm_{atm}^2) along with three mixing angles θ_{23} , θ_{12} and θ_{13} . Data

indicates that $|\Delta m_{atm}^2| \gg \Delta m_{\odot}^2$, but depending on the sign of Δm_{atm}^2 , two cases can arise.

• **Normal Hierarchy (NH):**

$$\begin{cases} m_1 = 0 \\ m_2 = \sqrt{\Delta m_{\odot}^2} \ll m_3 = \sqrt{\Delta m_{atm}^2} \end{cases} \quad (7.8)$$

In Normal Hierarchy(NH), the lightest mass eigenstate $m_1 = 0$. So, in order for LHS of Eqn 7.7 *i.e.*, $Y_{1\alpha}$ to vanish, R_{12} and R_{13} must be zero, since m_2 and m_3 are non zero. The orthogonality of R then implies that $R_{11} = 1$ and $R_{21} = 0 = R_{31}$. The four remaining elements of R *viz.*, R_{22} , R_{23} , R_{32} and R_{33} , form a 2×2 complex orthogonal matrix, defined by one complex angle z [90]. Thus the structure of R matrix in case of NH is reduced to the simple form:

$$R = \begin{pmatrix} 1 & 0 & 0 \\ 0 & \cos z & -\sin z \\ 0 & \sin z & \cos z \end{pmatrix} \quad (7.9)$$

The neutrino Dirac mass matrix obtained has the form :

$$m_D = v \begin{pmatrix} 0 & 0 & 0 \\ Y_{2e} & Y_{2\mu} & Y_{2\tau} \\ Y_{3e} & Y_{3\mu} & Y_{3\tau} \end{pmatrix} \quad (7.10)$$

where each element $Y_{\alpha j}$ of m_D is given by Eqn. 7.6.

• **Inverted Hierarchy (IH):**

$$\begin{cases} m_3 = 0 \\ m_1 = \sqrt{\Delta m_{atm}^2}, \quad m_2 = \sqrt{\Delta m_{atm}^2 + \Delta m_{\odot}^2} \end{cases} \quad (7.11)$$

In the case of Inverted Hierarchy(IH), we need to set $m_3 = 0$. So in order for LHS of Eqn. 7.7 *i.e.*, $Y_{1\alpha}$ to vanish, R_{11} and R_{12} must be zero. Again, orthogonality of R demands $R_{13} = 1$ making the first row and the third column of R trivial. The four remaining elements of R *viz.*, R_{21} , R_{22} , R_{31} and R_{32} then form a 2×2 complex orthogonal matrix, defined by one complex angle z . Thus the structure of R matrix in case of IH is given by:

$$R = \begin{pmatrix} 0 & 0 & 1 \\ \cos z & -\sin z & 0 \\ \sin z & \cos z & 0 \end{pmatrix} \quad (7.12)$$

Again we get a Dirac mass matrix of the same structure as that of NH case, with each element given by Eqn. 7.6.

Now, we turn to comment on the charged lepton flavour violation under this parametrization. In particular we study the process $\mu \rightarrow e\gamma$. The branching ratio of this process is given by [91–95],

$$Br(\mu \rightarrow e\gamma) = \frac{\alpha_w^3 s_w^2}{256\pi^2} \frac{m_\mu^4}{M_W^4} \frac{m_\mu}{\Gamma_\mu} |G_\gamma^{\mu e}|^2 \quad (7.13)$$

where α_w is the weak coupling strength, s_w is the sin of Weinberg's angle, m_μ is the muon mass, M_W is the mass of W boson and $\Gamma_\mu \approx 2.996 \times 10^{-19} \text{ GeV}$ denotes the total decay width of muon. The factor $G_\gamma^{\mu e}$ is given by,

$$G_\gamma^{\mu e} = \sum_i U_{ei} U_{\mu i}^* G_\gamma(x_i) = \sum_j U_{eN_j} U_{\mu N_j}^* G_\gamma(x_{N_j}) \quad (7.14)$$

where, $x_i = \frac{m_{\nu_i}^2}{M_W^2}$ and $x_{N_j} = \frac{M_{N_j}^2}{M_W^2}$. where i (j) runs over total number of light (heavy) physical neutrino states. m_ν (M_N) denotes the mass of light (heavy) physical neutrinos and U_{ei} (U_{eN_i}) represents the mixing matrix elements of light (heavy) neutrinos. The loop integration factor $G_\gamma(x)$ is given by,

$$G_\gamma(x) = -\frac{x(2x^2 + 5x - 1)}{4(1 - x^3)} - \frac{2x^3}{2(1 - x^4)} \ln(x) \quad (7.15)$$

To study the dependence of this branching ratio on the right handed mass scale in light of Casas-Ibarra parameterization, we derive from 7.13 the following equation,

$$Br(\mu \rightarrow e\gamma) = \frac{\alpha_w^3 s_w^2}{256\pi^2} \frac{m_\mu^4}{M_W^4} \frac{m_\mu}{\Gamma_\mu} \frac{4}{M_R^4} G_\gamma^2(x_N) |(m_D^\dagger m_D)_{e\mu}|^2 \quad (7.16)$$

where M_R denotes the mass of the right handed neutrino states. For simplicity we assume the two right handed neutrinos to be degenerate and $M_N = M_R$. The matrix element $(m_D^\dagger m_D)_{e\mu}$ for NH and IH respectively can be written using Eqn. 7.6 as,

$$(m_D^\dagger m_D)_{e\mu} \Big|_{NH} = M_R [(m_2 U_{e2} U_{\mu 2}^* + m_3 U_{e3} U_{\mu 3}^*) \cosh(2Im[z]) + i\sqrt{m_2} \sqrt{m_3} (U_{e3} U_{\mu 2}^* - U_{e2} U_{\mu 3}^*) \sinh(2Im[z])] \quad (7.17)$$

$$(m_D^\dagger m_D)_{e\mu} \Big|_{IH} = M_R [(m_1 U_{e1} U_{\mu 1}^* + m_2 U_{e2} U_{\mu 2}^*) \cosh(2Im[z]) + i\sqrt{m_1} \sqrt{m_2} (U_{e2} U_{\mu 1}^* - U_{e1} U_{\mu 2}^*) \sinh(2Im[z])] \quad (7.18)$$

where $U_{\alpha i}$ are the PMNS matrix elements parametrized as in Eqn 7.4. In Eqn. 7.17 and 7.18, there are three free parameters namely M_R , $Im[z]$ and α all other quantities being measured by oscillation experiments within a range. In left panel of Fig. 25, we have shown the $Br(\mu \rightarrow e\gamma)$ as a function of heavy neutrino mass M_R and $Im[z]$ taking all oscillation parameters within their 3σ range as given in [96, 97] in case of NH. The Majorana phase α is varied between 0 to 2π . and the amplitude $|(m_D^\dagger m_D)_{e\mu}|$ is almost independent of phase α . We confronted our result with current most stringent bound from MEG experiment $Br(\mu \rightarrow e\gamma) \leq 4.2 \times 10^{-13}$ [98], represented by the contour in black colour in left panel of Fig. 25. The red contour shows the projected MEG-II sensitivity of $Br(\mu \rightarrow e\gamma) \sim 6 \times 10^{-14}$. The region above the black contour is ruled out by MEG experiment while the region below this contour provides us a wide allowed parameter space for $Br(\mu \rightarrow e\gamma)$ in the $M_R - Im[z]$ plane

simultaneously satisfying MEG limit and low scale neutrino phenomenology. Similar result has been obtained for IH as well. In the right panel of Fig. 25, we have shown $\log[Br(\mu \rightarrow e\gamma)]$ for two particular values of $Im[z]$, $Im[z] = 0$ and 10.

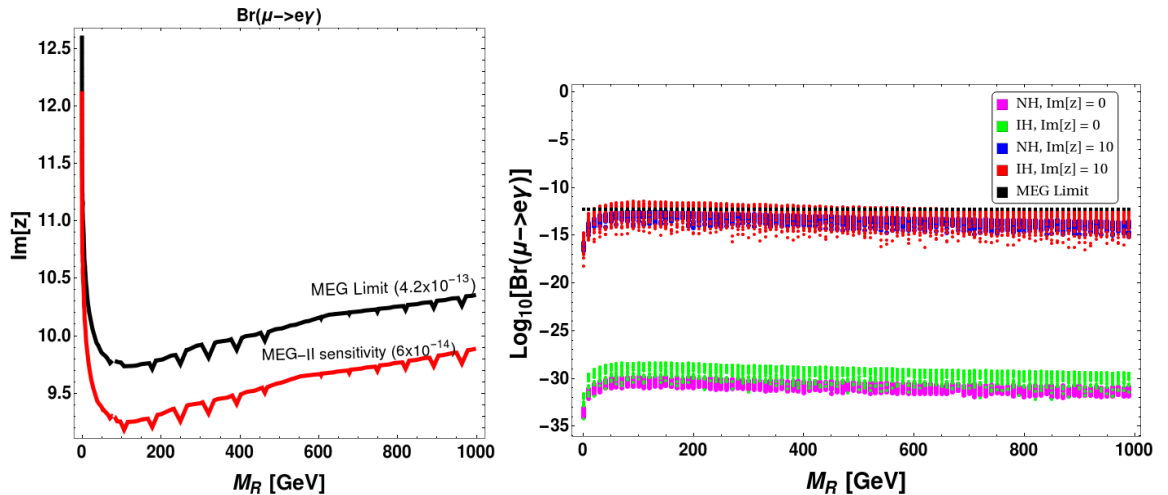


Figure 25: [Left]: $Br(\mu \rightarrow e\gamma)$ in $M_R - Im[z]$ plane; [Right]: $\text{Log}[Br(\mu \rightarrow e\gamma)]$ for $Im[z] = 0, 10$ for both NH and IH. The black dashed line represents the MEG limit.

In the simplest scenario $Im[z] = 0$, the branching ratio is very very less than the current sensitivity of worlds leading experiments like MEG for both NH and IH. For $Im[z] = 10$, the branching ratio is near to the current sensitivity. For intermediate values of $Im[z]$, $Br(\mu \rightarrow e\gamma)$ is below the current bound by MEG experiment, while for $Im[z] > 10$, $Br(\mu \rightarrow e\gamma)$ is above the MEG limit for almost all mass range of M_R upto 1000 GeV. As it can also be seen from the left panel of Fig. 25 that only for $M_R \leq 10$ GeV, $Im[z]$ can take values upto 14. Naturalness and vacuum stability bounds can also be applied in principle as done in [99], but these bounds are extremely weaker for M_R upto TeV scale.

8 Conclusion

In this paper, we have studied a minimal extension of the SM by adding a vector like fermion doublet Ψ and three singlet right handed neutrinos N_{R_i} to simultaneously address non-zero masses and mixing of light neutrinos as well as a phenomenologically viable dark matter component of the universe. An additional \mathcal{Z}_2 symmetry is required on top of the SM gauge symmetry to ensure the stability of the DM. Now, the \mathcal{Z}_2 symmetry crucially distinguishes the added fermions; for example, the vector-like fermion doublet and one of the three right handed neutrinos are assumed odd, while the rest are even. As a result the dark matter emerges as the lightest Majorana fermion from the mixture of the neutral component of the doublet Ψ and the singlet, which is odd under the same \mathcal{Z}_2 . The other two right handed neutrinos being even under the \mathcal{Z}_2 symmetry couple to SM Higgs and generate non-zero masses for light neutrinos via type-I seesaw. The absence of either the doublet or the singlet (odd under \mathcal{Z}_2), make the

DM absurdly constrained from relic density and direct search prospects. Therefore, one can simply see that the model under study is possibly the most economical one to simultaneously address neutrino mass and a phenomenologically viable DM candidate of the universe.

We studied the allowed parameter space of the model taking into account all annihilation and co-annihilation channels for DM mass ranging from 1 GeV to 1 TeV. The allowed parameter space is shown in the $\Delta M \sim m_{\chi_3}$ plane, where m_{χ_3} is the mass of the dark matter and ΔM is its mass difference with next to lightest dark sector particle. We confronted our results with recent data from both PLANCK and XENON-1T to obtain the correct parameter space satisfying both relic density and direct detection constraints. Since the DM is Majorana in nature, it escapes from the strong Z -mediated direct detection constraint. As a result we end up with relatively large singlet-doublet mixing. In particular, for DM mass of 1TeV, the allowed singlet-doublet mixing can be as large as $\sin \theta \sim 0.6$. This crucially distinguishes the Majorana singlet-doublet DM from a vector like singlet-doublet DM. This feature also hasn't been highlighted in earlier analysis of a similar model framework.

Since with three right handed neutrinos, the model is qualified for a anomaly-free gauged B-L extension, we studied how our results change in light of $U(1)_{B-L}$ gauge extension. Clearly, the model requires an additional complex scalar singlet to break the gauge group and the massive gauge boson Z_{BL} further enhances the DM-SM coupling. The relic density allowed parameter space additionally enhances due to Z_{BL} resonance in regions where $m_{DM} < M_{Z_{BL}}$. Also, the scalar sector mixes the SM doublet and additional singlet to produce two neutral scalar fields to mediate DM-SM interactions and enhance direct search possibility. The constraint on $g_{BL} - M_{Z_{BL}}$ from current LHC data is significant enough to ensure the coupling to be minuscule for relatively smaller $M_{Z_{BL}} \sim \text{TeV}$, so that the DM signal at LHC doesn't have any additional contribution from Z_{BL} mediation to ψ^\pm pair production. However with larger $M_{Z_{BL}} \sim 4 \text{ TeV}$, the coupling (g_{BL}) can be large enough to show up additional signal strength at LHC, which can be probed in its high luminosity run. It is worthy to mention that both the models offer variety of leptonic signatures like hadronically quiet opposite sign dilepton (OSD), trilepton or four lepton in association with missing energy. In a toy simulation for OSD events at LHC, we showed that it is easier to probe large ΔM regions of the model, characteristic to the $U(1)_{B-L}$ scenario than the small ΔM regions characteristic to the framework without $U(1)_{B-L}$. The model may also offer displaced vertex or stable charge track whenever the mass splitting ΔM between the charged companion and DM becomes very small.

Neutrino mass generation although fused naturally in this model, do not have direct influence on the dark sector. However, the RH neutrino mass turns out crucial for the neutrino sector, constrained from flavour changing decays like ($\mu \rightarrow e\gamma$). On the other hand, in the small mixing scenario, DM mass is dominantly controlled by the RH neutrino odd under \mathcal{Z}_2 symmetry *i.e.* $m_{DM} \sim M_{R_1}$. Since in the context of $U(1)_{B-L}$ model, the Majorana masses of all the three RH neutrinos (including the one in the dark sector) are generated uniformly from the same symmetry breaking scale, we can treat them as a common parameter of the framework constrained by both dark sector and neutrino sector as a bridging ligand of the model.

Acknowledgments : MD acknowledges Department of Science and Technology (DST), Govt. of India for providing the financial assistance for the research under the grant DST/INSPIRE/03/2017/000032. MD also acknowledges Anirban Karan for his help in learning some computational techniques. PG would like to acknowledge the support from DAE, India for the Regional Centre for Accelerator based Particle Physics(RECAPP), Harish Chandra Research Institute. SB would like to acknowledge to DST-SERB grant CRG/2019/004078 at IIT Guwahati.

Appendix

A DM-SM Interaction in model I

Expanding the covariant derivative of the Lagrangian given by Eq.2.1, we get the interaction term of ψ^0 and ψ^\pm with the SM gauge bosons as follows:

$$\begin{aligned}
\mathcal{L}_{int} &= \bar{\Psi} i \gamma^\mu \left(-i \frac{g}{2} \tau \cdot W_\mu - i g' \frac{Y}{2} B_\mu \right) \Psi \\
&= \left(\frac{e}{2 \sin \theta_W \cos \theta_W} \right) \bar{\psi}^0 \gamma^\mu Z_\mu \psi^0 \\
&+ \frac{e}{\sqrt{2} \sin \theta_W} (\bar{\psi}^0 \gamma^\mu W_\mu^+ \psi^- + \psi^+ \gamma^\mu W_\mu^- \psi^0) \\
&- e \psi^+ \gamma^\mu A_\mu \psi^- \\
&- \left(\frac{e \cos 2\theta_W}{2 \sin \theta_W \cos \theta_W} \right) \psi^+ \gamma^\mu Z_\mu \psi^-.
\end{aligned} \tag{A.1}$$

where $g = \frac{e}{\sin \theta_W}$ and $g' = \frac{e}{\cos \theta_W}$ with e being the electromagnetic coupling constant and θ_W being the Weinberg angle.

These interactions, when written in terms of the physical states becomes:

$$\begin{aligned}
\mathcal{L}_{int} &= \left(\frac{e}{2 \sin \theta_W \cos \theta_W} \right) (-\cos \theta_{\bar{\chi}_{1L}} i \gamma^\mu Z_\mu \chi_{2L} - \sin \theta_{\bar{\chi}_{2L}} i \gamma^\mu Z_\mu \chi_{3L} + h.c.) \\
&+ \frac{e}{\sqrt{2} \sin \theta_W} (\cos \theta_{\bar{\chi}_1} \gamma^\mu W_\mu^+ \psi^- + \bar{\chi}_2 i \gamma^\mu W_\mu^+ \psi^- - \sin \theta_{\bar{\chi}_3} \gamma^\mu W_\mu^+ \psi^-) \\
&+ \frac{e}{\sqrt{2} \sin \theta_W} (\cos \theta_{\psi^+} \gamma^\mu W_\mu^- \chi_1 - \psi^+ i \gamma^\mu W_\mu^- \chi_2 - \sin \theta_{\psi^+} \gamma^\mu W_\mu^- \chi_3) \\
&- e \psi^+ \gamma^\mu A_\mu \psi^- \\
&- \left(\frac{e \cos 2\theta_W}{2 \sin \theta_W \cos \theta_W} \right) \psi^+ \gamma^\mu Z_\mu \psi^-.
\end{aligned} \tag{A.2}$$

Another possibility of interaction between DM sector and the visible sector arises from the Yukawa interaction term $\frac{Y_1}{\sqrt{2}} \bar{\Psi} \tilde{H} (N_{R_1} + (N_{R_1})^c)$ and its hermitian conjugate by expanding the SM Higgs H around its vev. Writing in terms of physical bases,

$$-\mathcal{L}_{DM-Higgs} = \frac{Y_1}{\sqrt{2}} \left[\sin 2\theta (\bar{\chi}_1 h \chi_1 - \bar{\chi}_3 h \chi_3) + \cos 2\theta (\bar{\chi}_1 h \chi_3 + \bar{\chi}_3 h \chi_1) \right]. \tag{A.3}$$

Additionally, dark sector particles can annihilate into \mathcal{Z}_2 even right handed neutrino $N_{R_{2/3}}$ and SM neutrinos via the Yukawa term $\left(Y_{j\alpha}\overline{N_{R_j}}\tilde{H}^\dagger L_\alpha + h.c.\right)$ present in Eqn. 2.3. As it has been stated already, the lightest stable particle χ_3 serves as the DM. The relic abundance of χ_3 can be obtained through its annihilations to as well as through coannihilations with χ_1 , χ_2 and ψ^\pm to SM particles. The main processes which contribute to the relic abundance of DM are noted below:

$$\begin{aligned}
\overline{\chi_1}\chi_1 &\rightarrow hh, W^+W^-, ZZ, f\bar{f}, N_{R_{2/3}}\bar{\nu}_{e/\mu/\tau} \\
\overline{\chi_1}\chi_2 &\rightarrow hh, Zh, W^+W^-, ZZ, f\bar{f} \\
\overline{\chi_1}\chi_3 &\rightarrow hh, W^+W^-, ZZ, f\bar{f}, N_{R_{2/3}}\bar{\nu}_{e/\mu/\tau} \\
\overline{\chi_2}\chi_1 &\rightarrow hh, Zh, W^+W^-, ZZ, f\bar{f} \\
\overline{\chi_2}\chi_3 &\rightarrow hh, Zh, W^+W^-, ZZ, f\bar{f} \\
\overline{\chi_3}\chi_1 &\rightarrow hh, W^+W^-, ZZ, f\bar{f}, N_{R_{2/3}}\bar{\nu}_{e/\mu/\tau} \\
\overline{\chi_3}\chi_2 &\rightarrow hh, Zh, W^+W^-, ZZ, f\bar{f} \\
\overline{\chi_3}\chi_3 &\rightarrow hh, W^+W^-, ZZ, f\bar{f}, N_{R_{2/3}}\bar{\nu}_{e/\mu/\tau} \\
\chi_1\psi^\pm &\rightarrow W^\pm\gamma, W^\pm h, W^\pm Z, f'f \\
\chi_2\psi^\pm &\rightarrow W^\pm\gamma, W^\pm h, W^\pm Z, f'f \\
\chi_3\psi^\pm &\rightarrow W^\pm\gamma, W^\pm h, W^\pm Z, f'f \\
\psi^\pm\psi^\mp &\rightarrow W^\pm W^\mp, Zh, \gamma Z, \gamma\gamma, ZZ, f\bar{f}
\end{aligned}$$

B DM-SM Interaction in model II with $U(1)_{B-L}$ extension

The interaction terms of the dark and visible sector particles in the gauged $U(1)_{B-L}$ scenario can be obtained by expanding the kinetic terms of Ψ and N_{R_1} given in Eq.-5.3 as the following,

$$\begin{aligned}
\mathcal{L}_{int} &= \overline{\Psi}i\gamma^\mu[-i\frac{g}{2}\tau.W_\mu - ig'\frac{Y}{2}B_\mu - ig_{BL}Y_{BL}(Z_{BL})_\mu]\Psi \\
&\quad + \overline{N_{R_1}}i\gamma^\mu(-ig_{BL}Y_{BL}(Z_{BL})_\mu)N_{R_1} \\
&= \left(\frac{e}{2\sin\theta_W\cos\theta_W}\right)\overline{\psi^0}\gamma^\mu Z_\mu\psi^0 \\
&\quad + \frac{e}{\sqrt{2}\sin\theta_W}(\overline{\psi^0}\gamma^\mu W_\mu^+\psi^- + \psi^+\gamma^\mu W_\mu^-\psi^0) \\
&\quad - e\psi^+\gamma^\mu A_\mu\psi^- \\
&\quad - \left(\frac{e\cos 2\theta_W}{2\sin\theta_W\cos\theta_W}\right)\psi^+\gamma^\mu Z_\mu\psi^- \\
&\quad - g_{BL}\left[\overline{\psi^0}\gamma^\mu(Z_{BL})_\mu\psi^0 + \psi^+\gamma^\mu(Z_{BL})_\mu\psi^- + \overline{N_{R_1}}\gamma^\mu(Z_{BL})_\mu N_{R_1}\right].
\end{aligned} \tag{B.1}$$

where $g = \frac{e}{\sin\theta_W}$ and $g' = \frac{e}{\cos\theta_W}$ with e being the electromagnetic coupling constant, θ_W being the Weinberg angle and g_{BL} is the $U(1)_{B-L}$ coupling constant. The other interaction is through the Yukawa interaction term $Y_1\overline{\Psi}\tilde{H}N_{R_1}$, where we now have to also take into account

the mixing between H and Φ_{BL} . In terms of physical bases χ_1, χ_2 and χ_3 , the interaction terms of DM with the SM gauge bosons are given by:

$$\begin{aligned}
\mathcal{L}_{DM-SM} = & \left(\frac{e}{2 \sin \theta_W \cos \theta_W} \right) \left[(2s_{23}s_{13}c_{13})(\overline{\chi_{3L}}\gamma^\mu Z_\mu \chi_{3L} - \overline{\chi_{1L}}\gamma^\mu Z_\mu \chi_{1L}) \right. \\
& + (c_{23}c_{13}\overline{\chi_{1L}}\gamma^\mu Z_\mu \chi_{2L} - c_{213}s_{23}\overline{\chi_{1L}}\gamma^\mu Z_\mu \chi_{3L} - s_{13}c_{23}\overline{\chi_{2L}}\gamma^\mu Z_\mu \chi_{3L} + h.c.) \left. \right] \\
& + \frac{e}{\sqrt{2} \sin \theta_W} \left[\frac{1}{\sqrt{2}} \left((c_{13} - s_{13}s_{23})\overline{\chi_{1L}} + c_{23}\overline{\chi_{2L}} - (s_{13} + s_{23}c_{13})\overline{\chi_{3L}} \right) \gamma^\mu W_\mu^+ \psi_L^- \right. \\
& + \frac{1}{\sqrt{2}} \left((c_{13} + s_{13}s_{23})\overline{\chi_{1L}} - c_{23}\overline{\chi_{2L}} - (s_{13} - s_{23}c_{13})\overline{\chi_{3L}} \right) \gamma^\mu W_\mu^+ \psi_R^- + h.c. \left. \right] \\
& - e \psi^+ \gamma^\mu A_\mu \psi^- - \left(\frac{e \cos 2\theta_W}{2 \sin \theta_W \cos \theta_W} \right) \psi^+ \gamma^\mu Z_\mu \psi^-.
\end{aligned} \tag{B.2}$$

Additionally we have the interactions of DM with Z_{BL} as follows:

$$\begin{aligned}
\mathcal{L}_{DM-Z_{BL}} = & -g_{BL} \left[(s_{23}s_{213} + c_{13}^2 c_{23}^2)(\overline{\chi_{3L}}\gamma^\mu (Z_{BL})_\mu \chi_{3L} \right. \\
& + (s_{13}^2 c_{23}^2 - s_{23}s_{213})\overline{\chi_{1L}}\gamma^\mu (Z_{BL})_\mu \chi_{1L} + s_{23}^2 \overline{\chi_{2L}}\gamma^\mu (Z_{BL})_\mu \chi_{2L} \\
& + \left(\frac{1}{2} s_{223}s_{13} + c_{23}c_{13} \right) (\overline{\chi_{1L}}\gamma^\mu (Z_{BL})_\mu \chi_{2L} + h.c.) \\
& + \left(\frac{1}{2} s_{213}c_{23}^2 - c_{213}s_{23} \right) (\overline{\chi_{1L}}\gamma^\mu (Z_{BL})_\mu \chi_{3L} + h.c.) \\
& + \left. \left(\frac{1}{2} s_{223}c_{13} - s_{13}c_{23} \right) \overline{\chi_{2L}}\gamma^\mu (Z_{BL})_\mu \chi_{3L} + h.c. \right] \\
& - g_{BL} \psi^+ \gamma^\mu (Z_{BL})_\mu \psi^-.
\end{aligned} \tag{B.3}$$

Here, we abbreviated $\sin 2\theta_{ij}$ and $\cos 2\theta_{ij}$ as s_{2ij} and c_{2ij} respectively. We note that in the limit $\sin \theta_{23} \rightarrow 0$ (along with $g_{BL} \rightarrow 0$), we get back to the interactions present in A.2. DM-Scalar interaction also have additional channels from H and Φ_{B-L} mixing given by,

$$\begin{aligned}
-\mathcal{L}_{DM-Higgs} = & \frac{Y_1}{2} (h_1 \cos \beta - h_2 \sin \beta) \left[\left((c_{13} - s_{13}s_{23})\overline{\chi_{1L}} + c_{23}\overline{\chi_{2L}} - (s_{13} + s_{23}c_{13})\overline{\chi_{3L}} \right) \right. \\
& \left. \left(s_{13}c_{23}(\chi_{1L})^c + s_{23}(\chi_{2L})^c + c_{13}c_{23}(\chi_{3L})^c \right) + h.c. \right] \\
& + \frac{y'_1}{2\sqrt{2}} (h_2 \cos \beta + h_1 \sin \beta) \left[\left(s_{13}c_{23}(\chi_{1L})^c + s_{23}(\chi_{2L})^c + c_{13}c_{23}(\chi_{3L})^c \right) \right. \\
& \left. \left(s_{13}c_{23}\chi_{1L} + s_{23}\chi_{2L} + c_{13}c_{23}\chi_{3L} \right) + h.c. \right],
\end{aligned} \tag{B.4}$$

where h_1, h_2 are the two physical scalars of the model and β represents $H - \Phi_{B-L}$ mixing angle. The annihilation channels of dark matter in the $U(1)_{B-L}$ extended case differs from the one without it, by having additional Z_{BL} and an additional scalar present both in mediator as well as in final states. The following processes contributes to the relic abundance of the DM particle χ_3 in this model with $U(1)_{B-L}$ extension.

$$\begin{aligned}
\bar{\chi}_1 \chi_1 &\rightarrow h_1 h_1, h_2 h_2, h_1 h_2, W^+ W^-, ZZ, Z_{BL} Z_{BL}, ZZ_{BL}, f\bar{f}, N_{R_{2/3}} N_{R_{2/3}}, N_{R_{2/3}} \bar{\nu}_{e/\mu/\tau} \\
\bar{\chi}_1 \chi_2 &\rightarrow h_1 h_1, h_2 h_2, h_1 h_2, Zh_1, Zh_2, Z_{BL} h_1, Z_{BL} h_2, W^+ W^-, ZZ, Z_{BL} Z_{BL}, ZZ_{BL}, f\bar{f}, N_{R_{2/3}} N_{R_{2/3}}, N_{R_{2/3}} \bar{\nu}_{e/\mu/\tau} \\
\bar{\chi}_1 \chi_3 &\rightarrow h_1 h_1, h_2 h_2, h_1 h_2, W^+ W^-, ZZ, Z_{BL} Z_{BL}, ZZ_{BL}, f\bar{f}, N_{R_{2/3}} N_{R_{2/3}}, N_{R_{2/3}} \bar{\nu}_{e/\mu/\tau} \\
\bar{\chi}_2 \chi_1 &\rightarrow h_1 h_1, h_2 h_2, h_1 h_2, Zh_1, Zh_2, Z_{BL} h_1, Z_{BL} h_2, W^+ W^-, ZZ, Z_{BL} Z_{BL}, ZZ_{BL}, f\bar{f}, N_{R_{2/3}} N_{R_{2/3}}, N_{R_{2/3}} \bar{\nu}_{e/\mu/\tau} \\
\bar{\chi}_2 \chi_2 &\rightarrow h_1 h_1, h_2 h_2, h_1 h_2, Zh_1, Zh_2, Z_{BL} h_1, Z_{BL} h_2, W^+ W^-, ZZ, Z_{BL} Z_{BL}, ZZ_{BL}, f\bar{f}, N_{R_{2/3}} N_{R_{2/3}}, N_{R_{2/3}} \bar{\nu}_{e/\mu/\tau} \\
\bar{\chi}_2 \chi_3 &\rightarrow h_1 h_1, h_2 h_2, h_1 h_2, Zh_1, Zh_2, Z_{BL} h_1, Z_{BL} h_2, W^+ W^-, ZZ, Z_{BL} Z_{BL}, ZZ_{BL}, f\bar{f}, N_{R_{2/3}} N_{R_{2/3}}, N_{R_{2/3}} \bar{\nu}_{e/\mu/\tau} \\
\bar{\chi}_3 \chi_1 &\rightarrow h_1 h_1, h_2 h_2, h_1 h_2, W^+ W^-, ZZ, Z_{BL} Z_{BL}, ZZ_{BL}, f\bar{f}, N_{R_{2/3}} N_{R_{2/3}}, N_{R_{2/3}} \bar{\nu}_{e/\mu/\tau} \\
\bar{\chi}_3 \chi_2 &\rightarrow h_1 h_1, h_2 h_2, h_1 h_2, Zh_1, Zh_2, Z_{BL} h_1, Z_{BL} h_2, W^+ W^-, ZZ, Z_{BL} Z_{BL}, ZZ_{BL}, f\bar{f}, N_{R_{2/3}} N_{R_{2/3}}, N_{R_{2/3}} \bar{\nu}_{e/\mu/\tau} \\
\bar{\chi}_3 \chi_3 &\rightarrow h_1 h_1, h_2 h_2, h_1 h_2, W^+ W^-, ZZ, Z_{BL} Z_{BL}, ZZ_{BL}, f\bar{f}, N_{R_{2/3}} N_{R_{2/3}}, N_{R_{2/3}} \bar{\nu}_{e/\mu/\tau} \\
\chi_1 \psi^\pm &\rightarrow W^\pm \gamma, W^\pm h_1, W^\pm h_1, W^\pm Z, W^\pm Z_{BL}, f' f \\
\chi_2 \psi^\pm &\rightarrow W^\pm \gamma, W^\pm h_1, W^\pm h_1, W^\pm Z, W^\pm Z_{BL}, f' f \\
\chi_3 \psi^\pm &\rightarrow W^\pm \gamma, W^\pm h_1, W^\pm h_1, W^\pm Z, W^\pm Z_{BL}, f' f \\
\psi^\pm \psi^\mp &\rightarrow W^\pm W^\mp, Zh_1, Zh_2, Z_{BL} h_1, Z_{BL} h_2, \gamma Z, \gamma \gamma, ZZ, Z_{BL} Z_{BL}, ZZ_{BL}, f\bar{f}
\end{aligned}$$

References

- [1] G. Bertone, D. Hooper, and J. Silk, *Particle dark matter: Evidence, candidates and constraints*, *Phys. Rept.* **405** (2005) 279–390, [[hep-ph/0404175](#)].
- [2] G. Jungman, M. Kamionkowski, and K. Griest, *Supersymmetric dark matter*, *Phys. Rept.* **267** (1996) 195–373, [[hep-ph/9506380](#)].
- [3] **WMAP** Collaboration, G. Hinshaw et al., *Nine-Year Wilkinson Microwave Anisotropy Probe (WMAP) Observations: Cosmological Parameter Results*, *Astrophys. J. Suppl.* **208** (2013) 19, [[arXiv:1212.5226](#)].
- [4] **Planck** Collaboration, P. Ade et al., *Planck 2013 results. XVI. Cosmological parameters*, *Astron. Astrophys.* **571** (2014) A16, [[arXiv:1303.5076](#)].
- [5] E. W. Kolb and M. S. Turner, *The Early Universe*, vol. 69. 1990.
- [6] **T2K** Collaboration, K. Abe et al., *Indication of Electron Neutrino Appearance from an Accelerator-produced Off-axis Muon Neutrino Beam*, *Phys. Rev. Lett.* **107** (2011) 041801, [[arXiv:1106.2822](#)].
- [7] **T2K** Collaboration, K. Abe et al., *Observation of Electron Neutrino Appearance in a Muon Neutrino Beam*, *Phys. Rev. Lett.* **112** (2014) 061802, [[arXiv:1311.4750](#)].
- [8] **Double Chooz** Collaboration, Y. Abe et al., *Indication of Reactor $\bar{\nu}_e$ Disappearance in the Double Chooz Experiment*, *Phys. Rev. Lett.* **108** (2012) 131801, [[arXiv:1112.6353](#)].
- [9] **Double Chooz** Collaboration, H. de Kerret et al., *First Double Chooz θ_{13} Measurement via Total Neutron Capture Detection*, *Nature Phys.* **16** (2020), no. 5 558–564, [[arXiv:1901.09445](#)].
- [10] **Daya Bay** Collaboration, F. An et al., *Observation of electron-antineutrino disappearance at Daya Bay*, *Phys. Rev. Lett.* **108** (2012) 171803, [[arXiv:1203.1669](#)].
- [11] **Daya Bay** Collaboration, F. An et al., *Evolution of the Reactor Antineutrino Flux and Spectrum at Daya Bay*, *Phys. Rev. Lett.* **118** (2017), no. 25 251801, [[arXiv:1704.01082](#)].

- [12] **Daya Bay** Collaboration, D. Adey et al., *Measurement of the Electron Antineutrino Oscillation with 1958 Days of Operation at Daya Bay*, *Phys. Rev. Lett.* **121** (2018), no. 24 241805, [[arXiv:1809.02261](#)].
- [13] **RENO** Collaboration, J. Ahn et al., *Observation of Reactor Electron Antineutrino Disappearance in the RENO Experiment*, *Phys. Rev. Lett.* **108** (2012) 191802, [[arXiv:1204.0626](#)].
- [14] **MINOS** Collaboration, P. Adamson et al., *Measurement of Neutrino and Antineutrino Oscillations Using Beam and Atmospheric Data in MINOS*, *Phys. Rev. Lett.* **110** (2013), no. 25 251801, [[arXiv:1304.6335](#)].
- [15] **MINOS** Collaboration, P. Adamson et al., *Combined analysis of ν_μ disappearance and $\nu_\mu \rightarrow \nu_e$ appearance in MINOS using accelerator and atmospheric neutrinos*, *Phys. Rev. Lett.* **112** (2014) 191801, [[arXiv:1403.0867](#)].
- [16] **CUPID-0** Collaboration, O. Azzolini et al., *First Result on the Neutrinoless Double- β Decay of ^{82}Se with CUPID-0*, *Phys. Rev. Lett.* **120** (2018), no. 23 232502, [[arXiv:1802.07791](#)].
- [17] S. Weinberg, *Baryon and Lepton Nonconserving Processes*, *Phys. Rev. Lett.* **43** (1979) 1566–1570.
- [18] P. Minkowski, *$\mu \rightarrow e\gamma$ at a Rate of One Out of 10^9 Muon Decays?*, *Phys. Lett. B* **67** (1977) 421–428.
- [19] T. Yanagida, *NEUTRINO MASS AND HORIZONTAL SYMMETRY.*, in *1981 INS Symposium on Quark and Lepton Physics*, pp. 233–237, 1, 1981.
- [20] M. Gell-Mann, P. Ramond, and R. Slansky, *Complex Spinors and Unified Theories*, *Conf. Proc. C* **790927** (1979) 315–321, [[arXiv:1306.4669](#)].
- [21] R. N. Mohapatra and G. Senjanovic, *Neutrino Mass and Spontaneous Parity Nonconservation*, *Phys. Rev. Lett.* **44** (1980) 912.
- [22] N. Arkani-Hamed, S. Dimopoulos, and S. Kachru, *Predictive landscapes and new physics at a TeV*, [hep-th/0501082](#).
- [23] A. Freitas, S. Westhoff, and J. Zupan, *Integrating in the Higgs Portal to Fermion Dark Matter*, *JHEP* **09** (2015) 015, [[arXiv:1506.04149](#)].
- [24] G. Cynolter, J. Kovács, and E. Lendvai, *Doublet–singlet model and unitarity*, *Mod. Phys. Lett. A* **31** (2016), no. 01 1650013, [[arXiv:1509.05323](#)].
- [25] L. Calibbi, A. Mariotti, and P. Tziveloglou, *Singlet-Doublet Model: Dark matter searches and LHC constraints*, *JHEP* **10** (2015) 116, [[arXiv:1505.03867](#)].
- [26] T. Abe, R. Kitano, and R. Sato, *Discrimination of dark matter models in future experiments*, *Phys. Rev. D* **91** (2015), no. 9 095004, [[arXiv:1411.1335](#)]. [Erratum: *Phys.Rev.D* 96, 019902 (2017)].
- [27] C. Cheung and D. Sanford, *Simplified Models of Mixed Dark Matter*, *JCAP* **02** (2014) 011, [[arXiv:1311.5896](#)].
- [28] T. Cohen, J. Kearney, A. Pierce, and D. Tucker-Smith, *Singlet-Doublet Dark Matter*, *Phys. Rev. D* **85** (2012) 075003, [[arXiv:1109.2604](#)].
- [29] R. Enberg, P. Fox, L. Hall, A. Papaioannou, and M. Papucci, *LHC and dark matter signals of improved naturalness*, *JHEP* **11** (2007) 014, [[arXiv:0706.0918](#)].

- [30] F. D’Eramo, *Dark matter and Higgs boson physics*, *Phys. Rev. D* **76** (2007) 083522, [[arXiv:0705.4493](#)].
- [31] R. Mahbubani and L. Senatore, *The Minimal model for dark matter and unification*, *Phys. Rev. D* **73** (2006) 043510, [[hep-ph/0510064](#)].
- [32] S. Banerjee, S. Matsumoto, K. Mukaida, and Y.-L. S. Tsai, *WIMP Dark Matter in a Well-Tempered Regime: A case study on Singlet-Doublets Fermionic WIMP*, *JHEP* **11** (2016) 070, [[arXiv:1603.07387](#)].
- [33] A. Dutta Banik, A. K. Saha, and A. Sil, *Scalar assisted singlet doublet fermion dark matter model and electroweak vacuum stability*, *Phys. Rev. D* **98** (2018), no. 7 075013, [[arXiv:1806.08080](#)].
- [34] S. Horiuchi, O. Macias, D. Restrepo, A. Rivera, O. Zapata, and H. Silverwood, *The Fermi-LAT gamma-ray excess at the Galactic Center in the singlet-doublet fermion dark matter model*, *JCAP* **03** (2016) 048, [[arXiv:1602.04788](#)].
- [35] D. Restrepo, A. Rivera, M. Sánchez-Peláez, O. Zapata, and W. Tangarife, *Radiative Neutrino Masses in the Singlet-Doublet Fermion Dark Matter Model with Scalar Singlets*, *Phys. Rev. D* **92** (2015), no. 1 013005, [[arXiv:1504.07892](#)].
- [36] M. Badziak, M. Olechowski, and P. Szczerbiak, *Is well-tempered neutralino in MSSM still alive after 2016 LUX results?*, *Phys. Lett. B* **770** (2017) 226–235, [[arXiv:1701.05869](#)].
- [37] A. Betancur, G. Palacio, and A. Rivera, *Inert doublet as multicomponent dark matter*, [[arXiv:2002.02036](#)].
- [38] T. Abe and R. Sato, *Current status and future prospects of the singlet-doublet dark matter model with CP-violation*, *Phys. Rev. D* **99** (2019), no. 3 035012, [[arXiv:1901.02278](#)].
- [39] T. Abe, *Effect of CP violation in the singlet-doublet dark matter model*, *Phys. Lett. B* **771** (2017) 125–130, [[arXiv:1702.07236](#)].
- [40] S. Bhattacharya, N. Sahoo, and N. Sahu, *Singlet-Doublet Fermionic Dark Matter, Neutrino Mass and Collider Signatures*, *Phys. Rev. D* **96** (2017), no. 3 035010, [[arXiv:1704.03417](#)].
- [41] B. Barman, S. Bhattacharya, P. Ghosh, S. Kadam, and N. Sahu, *Fermion Dark Matter with Scalar Triplet at Direct and Collider Searches*, *Phys. Rev. D* **100** (2019), no. 1 015027, [[arXiv:1902.01217](#)].
- [42] S. Bhattacharya, P. Ghosh, and N. Sahu, *Multipartite Dark Matter with Scalars, Fermions and signatures at LHC*, *JHEP* **02** (2019) 059, [[arXiv:1809.07474](#)].
- [43] S. Bhattacharya, B. Karmakar, N. Sahu, and A. Sil, *Flavor origin of dark matter and its relation with leptonic nonzero θ_{13} and Dirac CP phase δ* , *JHEP* **05** (2017) 068, [[arXiv:1611.07419](#)].
- [44] S. Bhattacharya, N. Sahoo, and N. Sahu, *Minimal vectorlike leptonic dark matter and signatures at the LHC*, *Phys. Rev. D* **93** (2016), no. 11 115040, [[arXiv:1510.02760](#)].
- [45] S. Bhattacharya, P. Ghosh, N. Sahoo, and N. Sahu, *Mini Review on Vector-Like Leptonic Dark Matter, Neutrino Mass, and Collider Signatures*, *Front. in Phys.* **7** (2019) 80, [[arXiv:1812.06505](#)].
- [46] P. Konar, A. Mukherjee, A. K. Saha, and S. Show, *A dark clue to seesaw and leptogenesis in singlet doublet scenario with (non)standard cosmology*, [[arXiv:2007.15608](#)].
- [47] **DELPHI** Collaboration, J. Abdallah et al., *Searches for supersymmetric particles in e^+e^-*

- collisions up to 208-GeV and interpretation of the results within the MSSM, *Eur. Phys. J. C* **31** (2003) 421–479, [[hep-ex/0311019](#)].
- [48] CMS Collaboration, A. M. Sirunyan et al., *Search for Evidence of the Type-III Seesaw Mechanism in Multilepton Final States in Proton-Proton Collisions at $\sqrt{s} = 13$ TeV*, *Phys. Rev. Lett.* **119** (2017), no. 22 221802, [[arXiv:1708.07962](#)].
- [49] CMS Collaboration, A. M. Sirunyan et al., *Search for physics beyond the standard model in multilepton final states in proton-proton collisions at $\sqrt{s} = 13$ TeV*, *JHEP* **03** (2020) 051, [[arXiv:1911.04968](#)].
- [50] XENON Collaboration, E. Aprile et al., *Dark Matter Search Results from a One Ton-Year Exposure of XENON1T*, *Phys. Rev. Lett.* **121** (2018), no. 11 111302, [[arXiv:1805.12562](#)].
- [51] XENON Collaboration, E. Aprile et al., *Observation of Excess Electronic Recoil Events in XENON1T*, [[arXiv:2006.09721](#)].
- [52] K. Griest and D. Seckel, *Three exceptions in the calculation of relic abundances*, *Phys. Rev. D* **43** (1991) 3191–3203.
- [53] A. Chatterjee and N. Sahu, *Resurrecting L-type sneutrino dark matter in light of neutrino masses and LUX data*, *Phys. Rev. D* **90** (2014), no. 9 095021, [[arXiv:1407.3030](#)].
- [54] S. Patra, N. Sahoo, and N. Sahu, *Dipolar dark matter in light of the 3.5 keV x-ray line, neutrino mass, and LUX data*, *Phys. Rev. D* **91** (2015), no. 11 115013, [[arXiv:1412.4253](#)].
- [55] G. Belanger, F. Boudjema, A. Pukhov, and A. Semenov, *Dark matter direct detection rate in a generic model with micrOMEGAs 2.2*, *Comput. Phys. Commun.* **180** (2009) 747–767, [[arXiv:0803.2360](#)].
- [56] N. D. Christensen and C. Duhr, *FeynRules - Feynman rules made easy*, *Comput. Phys. Commun.* **180** (2009) 1614–1641, [[arXiv:0806.4194](#)].
- [57] A. Alloul, N. D. Christensen, C. Degrande, C. Duhr, and B. Fuks, *FeynRules 2.0 - A complete toolbox for tree-level phenomenology*, *Comput. Phys. Commun.* **185** (2014) 2250–2300, [[arXiv:1310.1921](#)].
- [58] S. Jana, N. Okada, and D. Raut, *Displaced Vertex and Disappearing Track Signatures in type-III Seesaw*, [[arXiv:1911.09037](#)].
- [59] J. Alarcon, L. Geng, J. Martin Camalich, and J. Oller, *The strangeness content of the nucleon from effective field theory and phenomenology*, *Phys. Lett. B* **730** (2014) 342–346, [[arXiv:1209.2870](#)].
- [60] T. Gherghetta, J. Kersten, K. Olive, and M. Pospelov, *Evaluating the price of tiny kinetic mixing*, *Phys. Rev. D* **100** (2019), no. 9 095001, [[arXiv:1909.00696](#)].
- [61] Y. Mambrini, *The ZZ' kinetic mixing in the light of the recent direct and indirect dark matter searches*, *JCAP* **07** (2011) 009, [[arXiv:1104.4799](#)].
- [62] K. Kannike, *Vacuum Stability Conditions From Copositivity Criteria*, *Eur. Phys. J. C* **72** (2012) 2093, [[arXiv:1205.3781](#)].
- [63] J. Chakraborty, P. Konar, and T. Mondal, *Copositive Criteria and Boundedness of the Scalar Potential*, *Phys. Rev. D* **89** (2014), no. 9 095008, [[arXiv:1311.5666](#)].
- [64] G. Cacciapaglia, C. Csaki, G. Marandella, and A. Strumia, *The Minimal Set of Electroweak Precision Parameters*, *Phys. Rev. D* **74** (2006) 033011, [[hep-ph/0604111](#)].

- [65] **ATLAS** Collaboration, M. Aaboud et al., *Search for new high-mass phenomena in the dilepton final state using 36 fb^{-1} of proton-proton collision data at $\sqrt{s} = 13\text{ TeV}$ with the ATLAS detector*, *JHEP* **10** (2017) 182, [[arXiv:1707.02424](#)].
- [66] **CMS** Collaboration, A. M. Sirunyan et al., *Search for narrow and broad dijet resonances in proton-proton collisions at $\sqrt{s} = 13\text{ TeV}$ and constraints on dark matter mediators and other new particles*, *JHEP* **08** (2018) 130, [[arXiv:1806.00843](#)].
- [67] N. Okada and S. Okada, *Z'_{BL} portal dark matter and LHC Run-2 results*, *Phys. Rev. D* **93** (2016), no. 7 075003, [[arXiv:1601.07526](#)].
- [68] S. Bhattacharya, N. Chakrabarty, R. Roshan, and A. Sil, *Multicomponent dark matter in extended $U(1)_{B-L}$: neutrino mass and high scale validity*, *JCAP* **04** (2020) 013, [[arXiv:1910.00612](#)].
- [69] D. López-Val and T. Robens, *Δr and the W -boson mass in the singlet extension of the standard model*, *Phys. Rev. D* **90** (2014) 114018, [[arXiv:1406.1043](#)].
- [70] T. Robens and T. Stefaniak, *LHC Benchmark Scenarios for the Real Higgs Singlet Extension of the Standard Model*, *Eur. Phys. J. C* **76** (2016), no. 5 268, [[arXiv:1601.07880](#)].
- [71] **ATLAS** Collaboration, *Prospects for searches for staus, charginos and neutralinos at the high luminosity LHC with the ATLAS Detector*, .
- [72] L. Calibbi, J. M. Lindert, T. Ota, and Y. Takanishi, *Lhc tests of light neutralino dark matter without light sfermions*, *Journal of High Energy Physics* **2014** (Nov, 2014).
- [73] M. Abdughani, L. Wu, and J. M. Yang, *Status and prospects of light bino–higgsino dark matter in natural SUSY*, *Eur. Phys. J. C* **78** (2018), no. 1 4, [[arXiv:1705.09164](#)].
- [74] Q.-F. Xiang, X.-J. Bi, P.-F. Yin, and Z.-H. Yu, *Searching for Singlino-Higgsino Dark Matter in the NMSSM*, *Phys. Rev. D* **94** (2016), no. 5 055031, [[arXiv:1606.02149](#)].
- [75] G. Bélanger, G. Drieu La Rochelle, B. Dumont, R. M. Godbole, S. Kraml, and S. Kulkarni, *LHC constraints on light neutralino dark matter in the MSSM*, *Phys. Lett. B* **726** (2013) 773–780, [[arXiv:1308.3735](#)].
- [76] A. Choudhury and S. Mondal, *Revisiting the Exclusion Limits from Direct Chargino-Neutralino Production at the LHC*, *Phys. Rev. D* **94** (2016), no. 5 055024, [[arXiv:1603.05502](#)].
- [77] J. Cao, Y. He, L. Shang, W. Su, and Y. Zhang, *Testing the light dark matter scenario of the MSSM at the LHC*, *JHEP* **03** (2016) 207, [[arXiv:1511.05386](#)].
- [78] **ATLAS** Collaboration, G. Aad et al., *Search for direct production of charginos, neutralinos and sleptons in final states with two leptons and missing transverse momentum in pp collisions at $\sqrt{s} = 8\text{ TeV}$ with the ATLAS detector*, *JHEP* **05** (2014) 071, [[arXiv:1403.5294](#)].
- [79] **ATLAS** Collaboration, *Search for direct chargino pair production with W -boson mediated decays in events with two leptons and missing transverse momentum at $\sqrt{s} = 13\text{ TeV}$ with the ATLAS detector*, .
- [80] **ATLAS Collaboration** Collaboration, *Prospects for searches for staus, charginos and neutralinos at the high luminosity LHC with the ATLAS Detector*, Tech. Rep. ATL-PHYS-PUB-2018-048, CERN, Geneva, Dec, 2018.
- [81] *Searches for supersymmetric particles in $e + e^-$ collisions up to 208 gev and interpretation of the results within the mssm*, *The European Physical Journal C* **31** (Dec, 2003).

- [82] B. Barman, D. Borah, P. Ghosh, and A. K. Saha, *Flavoured gauge extension of singlet-doublet fermionic dark matter: neutrino mass, high scale validity and collider signatures*, *JHEP* **10** (2019) 275, [[arXiv:1907.10071](#)].
- [83] G. Aad, T. Abajyan, B. Abbott, J. Abdallah, S. A. Khalek, O. Abdinov, R. Aben, B. Abi, M. Abolins, and et al., *Search for direct production of charginos and neutralinos in events with three leptons and missing transverse momentum in $\sqrt{s}=8$ tev pp collisions with the atlas detector*, *Journal of High Energy Physics* **2014** (Apr, 2014).
- [84] S. K. Majee and N. Sahu, *Dilepton Signal of a Type-II Seesaw at CERN LHC: Reveals a TeV Scale B-L Symmetry*, *Phys. Rev. D* **82** (2010) 053007, [[arXiv:1004.0841](#)].
- [85] J. Alwall, M. Herquet, F. Maltoni, O. Mattelaer, and T. Stelzer, *MadGraph 5 : Going Beyond*, *JHEP* **06** (2011) 128, [[arXiv:1106.0522](#)].
- [86] T. Sjostrand, S. Mrenna, and P. Z. Skands, *PYTHIA 6.4 Physics and Manual*, *JHEP* **05** (2006) 026, [[hep-ph/0603175](#)].
- [87] J. Alwall, R. Frederix, S. Frixione, V. Hirschi, F. Maltoni, O. Mattelaer, H.-S. Shao, T. Stelzer, P. Torrielli, and M. Zaro, *The automated computation of tree-level and next-to-leading order differential cross sections, and their matching to parton shower simulations*, *Journal of High Energy Physics* **2014** (Jul, 2014).
- [88] J. Valle, *Neutrino physics overview*, *J. Phys. Conf. Ser.* **53** (2006) 473–505, [[hep-ph/0608101](#)].
- [89] J. Casas and A. Ibarra, *Oscillating neutrinos and $\mu \rightarrow e, \gamma$* , *Nucl. Phys. B* **618** (2001) 171–204, [[hep-ph/0103065](#)].
- [90] N. Narendra, N. Sahu, and S. U. Sankar, *Flavoured CP-asymmetry at the effective neutrino mass floor*, [[arXiv:2002.08753](#)].
- [91] R. Alonso, M. Dhen, M. Gavela, and T. Hambye, *Muon conversion to electron in nuclei in type-I seesaw models*, *JHEP* **01** (2013) 118, [[arXiv:1209.2679](#)].
- [92] X. Marcano Imaz, *Lepton flavor violation from low scale seesaw neutrinos with masses reachable at the LHC*. PhD thesis, U. Autonoma, Madrid (main), 6, 2017. [[arXiv:1710.08032](#)].
- [93] A. Ilakovac and A. Pilaftsis, *Flavor violating charged lepton decays in seesaw-type models*, *Nucl. Phys. B* **437** (1995) 491, [[hep-ph/9403398](#)].
- [94] F. Deppisch and J. Valle, *Enhanced lepton flavor violation in the supersymmetric inverse seesaw model*, *Phys. Rev. D* **72** (2005) 036001, [[hep-ph/0406040](#)].
- [95] A. Ilakovac, *Lepton flavor violation in the standard model extended by heavy singlet Dirac neutrinos*, *Phys. Rev. D* **62** (2000) 036010, [[hep-ph/9910213](#)].
- [96] F. Capozzi, E. Lisi, A. Marrone, and A. Palazzo, *Current unknowns in the three neutrino framework*, *Prog. Part. Nucl. Phys.* **102** (2018) 48–72, [[arXiv:1804.09678](#)].
- [97] **Particle Data Group** Collaboration, M. Tanabashi et al., *Review of Particle Physics*, *Phys. Rev. D* **98** (2018), no. 3 030001.
- [98] **MEG** Collaboration, T. Mori, *Final Results of the MEG Experiment*, *Nuovo Cim. C* **39** (2017), no. 4 325, [[arXiv:1606.08168](#)].
- [99] G. Bambhaniya, P. Bhupal Dev, S. Goswami, S. Khan, and W. Rodejohann, *Naturalness, Vacuum Stability and Leptogenesis in the Minimal Seesaw Model*, *Phys. Rev. D* **95** (2017), no. 9 095016, [[arXiv:1611.03827](#)].